SYNTHESIS OF FERROELECTRIC TWO DIMENSIONAL MATERIALS AND ITS HETEROSTRUCTURE

TSANG CHI SHING BEN

MPhil

The Hong Kong Polytechnic University

2024

The Hong Kong Polytechnic University

Department of Applied Physics

SYNTHESIS OF FERROELECTRIC TWO DIMENSIONAL MATERIALS AND ITS HETEROSTRUCTURE

TSANG Chi Shing Ben

A thesis submitted in partial fulfilment of the requirements for degree of Master of Philosophy

January 2024

CERTIFICATE OF ORIGINALITY

I hereby declare that this thesis is my own work and that, to the best of my knowledge and belief, it reproduces no material previously published or written, nor material that has been accepted for the award of any other degree or diploma, except where due acknowledgement has been made in the text.

________________________(Signed)

TSANG Chi Shing Ben (Name of Student)

Abstract

This thesis presents a study on the growth methods and latest research of three important two-dimensional materials: In_2Se_3, WS_2, and MoS_2, with a focus on their phase controllability and heterostructure synthesis mechanisms.

The study covers chemical vapor deposition (CVD) methods for the growth of different crystal phases of two-dimensional In_2Se_3 materials. Key aspects investigated include: (1) studying the mechanism for growing large-area In_2Se_3 during the growth process; (2) achieving phase modulation of In_2Se_3 through direct and indirect methods to create ferroelectric hybrid heterostructures with great potential in electronic devices; (3) synthesizing thin films of single-layer WS_2 and MoS_2 separately using molten salt assistance, analysing the influence of NaCl on film growth, and focusing on the growth of WS_2 to examine the growth conditions at different temperature. The study also explores the influence of growth processes on the interfaces and provides important insights for the investigation of nanoscale hybrid interfaces.

Initially, we prepared few-layer In_2Se_3 using chemical vapor deposition on 2D mica substrates and other templates. By adjusting the duration, sources amount, substrate distance, precursor. We obtained different morphologies and phases of In_2Se_3, with varying growth pathways. The morphological evolution from triangular flakes to layer-dependent shapes was observed through changes in conditions, which were confirmed using Raman spectroscopy to identify the phase transition. We concluded that the growth mechanism depends on the substrate. Furthermore, we systematically investigated the influence of precursor variation on domain size and surface coverage. By optimizing the growth conditions, we successfully grew β' In_2Se_3 and α In_2Se_3 thin films to gain a deeper understanding of the nanophase diagram of In_2Se_3, we further observed the dynamic phase transition of In_2Se_3 using optical polarized microscopy, identifying the in-situ

evolution from β'-In_2Se_3 to α-In_2Se_3 and elucidating the fundamental reasons for this phase transition. This led to the creation of ferroelectric hybrid heterostructures.

Our research focuses on the synthesis and analysis of two-dimensional materials such as In_2Se_3, MoS_2, and WS_2, which are poised to revolutionize semiconductor technologies as alternatives to silicon. Ferroelectric capabilities of In_2Se_3, and their electron mobility, are main reasons these materials were chosen for research. We investigate the chemical vapor deposition (CVD) methods to control the phase and growth of In_2Se_3, aiming to create ferroelectric hybrid phase heterostructures. Our investigation also extends to the effects of growth conditions on WS_2 and MoS_2, and the creation of WS_2-MoS_2 single-layer lateral heterostructures. Through this work, we have observed the dynamic phase transition of In_2Se_3 and uncovered the growth mechanisms dependent on substrate choice. The study confronts the challenges of synthesizing heterostructures with controllable interface and provides valuable insights into interfaces control and next-generation electronic devices.

Acknowledgements

With the completion of my thesis, my journey as an MPhil student comes to an end. Throughout this period, from conducting research to successfully completing the thesis, I have witnessed significant growth in my learning abilities and an expansion of my horizons. I would like to express my sincere gratitude to everyone who has taught and supported me during these years.

First, I am deeply grateful to my patient supervisor, Prof. Jiong Zhao. His serious attitude towards scientific research and profound knowledge in the field have greatly influenced my research journey, inspiring me to approach each challenge with enthusiasm. His guidance and constant encouragement have been invaluable, and I express my thanks to him.

I also thank my senior, Prof. Wei Han, who meticulously guided me through the synthesis of two-dimensional materials, sample preparation, characterization techniques, and laboratory protocols during my postgraduate and final year project. Without his kind assistance, this work could have been hardly finished.

I extend my gratitude to the members of Zhao research team, including Dr. Xiadong Zheng, Dr. Lok Wing Wong, Dr. Fangyuan Zheng, Mr. Ka Hei Lai, and Mr. Shan Jiang. Their insightful discussions and support in transmission electron microscopy and their valuable professional suggestions have greatly contributed to my research. I would also like to acknowledge Mr. Tianren Chen, Mr. Honglin Chen, and Hok Yin Wong for their assistance in laboratory maintenance and equipment support, as well as Mr. Zhangyuan Yuan for coding and software assistance. I feel fortunate to have received help from Prof. LY Thuc Hue, Prof. Ming Yang, Prof. Qiang Fu, Prof. Dengrong Sun, Dr. Haiyan Jin, Dr. Tong Yang, Ms. Wenqian Shen, and Mr. Haijun Liu.

I express my deepest appreciation to Dr. Wong Ho Fai, Dr. Terence Wong, Ms. Wing Man Ho, and Mr. Tsz Lam Chan for their invaluable maintenance in equipment utilization and safety regulations in the UMF and AP laboratories. I sincerely appreciate the executive support provided by Mr. Tiffany Wong.

I gratefully acknowledge the financial support from the Research Committee of The Hong Kong Polytechnic University throughout my academic journey.

Lastly, I would like to express my deepest gratitude to my parents for their endless love and unwavering support in my studies.

Tables of content

List of figures

List of Tables

List of publications

1. W. Han *et al.*, Phase-controllable large-area two-dimensional In2Se3 and ferroelectric heterophase junction. *Nature Nanotechnology* **18**, 55-63 (2023).
2. Y. Lin *et al.*, A Multiscale Deep-Learning Model for Atom Identification from Low-Signal-to-Noise-Ratio Transmission Electron Microscopy Images. *Small Science*, 2300031 (2023).
3. H. Y. Wong *et al.*, Superhydrophobic Surface Designing for Efficient Atmospheric Water Harvesting Aided by Intelligent Computer Vision. *ACS Applied Materials & Interfaces*, (2023).
4. X. Zheng *et al.*, Phase and polarization modulation in two-dimensional In2Se3 via in situ transmission electron microscopy. *Science advances* **8**, eabo0773 (2022).

List of abbreviations

TEM	Transmission Electron Microscopy	**AFM**	Atomic Force Microscopy
STEM	Scanning Transmission Electron Microscopy	**SEM**	Scanning Electron Microscopy
2D	Two-Dimensional	**CVD**	Chemical vapor deposition
Sccm	Standrad Cubic centimeter per minutes	**AP**	Atmospheric pressure Chemical Vapor deposition
vdW	Van Der Waals	**ALD**	Atomic layer deposition
HRTEM	High Resolution Transmission Electron Microscopy	**MBE**	Molecular beam expitaxy
SAED	Selected Area Electron Diffraction	**TMDs**	Transitional metal dichalcogenides
HAADF	High Angle Annular Dark Field	**FET**	Field effect transitor
Å	Angstrom	**nm**	manometer
eV	Electron Volt	**h-BN**	Hexagonal Boron Nitride
ML	monolayer	**BL**	Bilayer
PMMA	polymethylmethacrylate	**OM**	Optical Microscopy
DFT	Density Function Theory	**SiO_2/Si**	Silicon with silicon dioxide capped layer
HOPG	Highly Ordered Pyrolytic Graphite	**PDMS**	Polydimethylsiloxane

Chapter 1. Research Background

The rapid advancement of technology in the past few decades has been largely driven by the persistent pursuit of computational power, leading to the development of integrated electronics. Moore's Law, a prediction made by Gordon Moore in 1965, which states that the number of transistors on integrated circuits doubles approximately every 18 months(*19*). This exponential growth has increased the progress of various fields, including artificial intelligence, big data analytics, and intellectualization in daily life. As the demand for computational power continues to rise, the integration of a higher density of electronic components onto microchips has become imperative. However, this pursuit of increased integration has come with its own set of challenges. The manufacturing process has become increasingly complex, resulting in escalating fabrication costs and technological difficulties. Moreover, the size of traditional silicon-based semiconductor devices is rapidly approaching its physical limitations, as the channel thickness of silicon-based devices decreases to below 4 nm, it reaches a critical point where the physical limits of silicon start to hinder transmission speed and stability(*20*). Defects in the surface and interior of silicon can cause significant decreases in performance. Despite continuous advancements in manufacturing technologies, the future of silicon is predicted due to the quantum phenomenon of tunneling effect. This effect poses a significant challenge to Moore's Law(*19*), as it suggests that the termination of silicon.

To overcome the limitations of silicon-based devices, researchers have been exploring alternative materials that show promise in addressing these obstacles. Among them, two-dimensional (2D) materials have emerged as potential solutions, offering unique properties, including optical transparency(*21*), surface inactivity(*20, 22*), bandgap tunability(*23*), and structural compatibility of assemblies(*24*) that can enable size reduction and improved device performance.The 2D materials present opportunities for novel device architectures and functionalities that were previously unattainable with silicon-based technologies, making them potential replacements for silicon in integrated circuits. However, there are still challenges before these nanomaterials can replace silicon in manufacturing, such as massive production, cost-effectiveness, and integration with existing manufacturing processes which need to be addressed to realize their full potential(*22*).

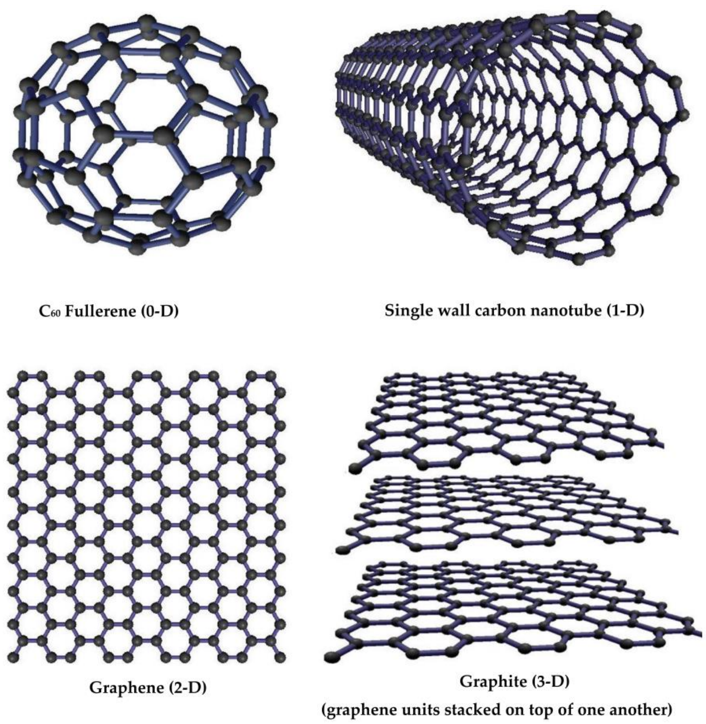

Figure 1 Depicts a schematic diagram illustrating the dimensional distinctions among nanomaterial categories, namely 0D, 1D, 2D, and 3D. Image from(*1*).

1.1 Two-dimensional family

The properties of materials can be influenced when their structures are confined in one or more dimensions. This confinement leads to various effects, such as the quantum size effect, surface effect, and quantum tunnelling, etc. These effects give rise to exceptional properties in mechanical, catalyst, optical, and electromagnetic aspects, making confined materials, commonly referred to as nanomaterials, a subject of great scientific interest and potential technological applications.

Nanomaterials are characterized by their size as shown in Figure 1, typically ranging from a few nanometers to a few hundred nanometers. At this scale, the fundamental properties of materials can deviate significantly from their bulk counterparts. One common type of (0D) nanomaterial is nanoparticles, which are clusters of atoms with no long-range order in three dimensions, typically measuring a few nanometers in size. These nanoparticles exhibit remarkable properties due to their high surface-to-volume ratio, allowing for enhanced reactivity, catalytic activity, and tailored surface functionalities. Another type of confined nanomaterial is nanofibers (1D), which are elongated structures with lengths on the order of hundreds of nanometers and diameters that are typically short in a few nanometers. These nanofibers exhibit exceptional mechanical strength, suitable for applications in which mechanical robustness is required. Thin-film (2D) materials represent a class of confined nanomaterials, typically a few nanometers thick. Such as graphene discovered by Novoselov in 2004(*21*). This groundbreaking achievement involved the use of Scotch tape to exfoliate a single layer of carbon, revealing the extraordinary properties of graphene.

In recent years, extensive research efforts have been dedicated to the study of graphene and other analogous 2D materials, including black phosphorus, transition metal dichalcogenides (TMD), III–V group elements, h-BN, metal organic framework, MXenes, and etc. Figure 1.1

brief to the 2D material classes.

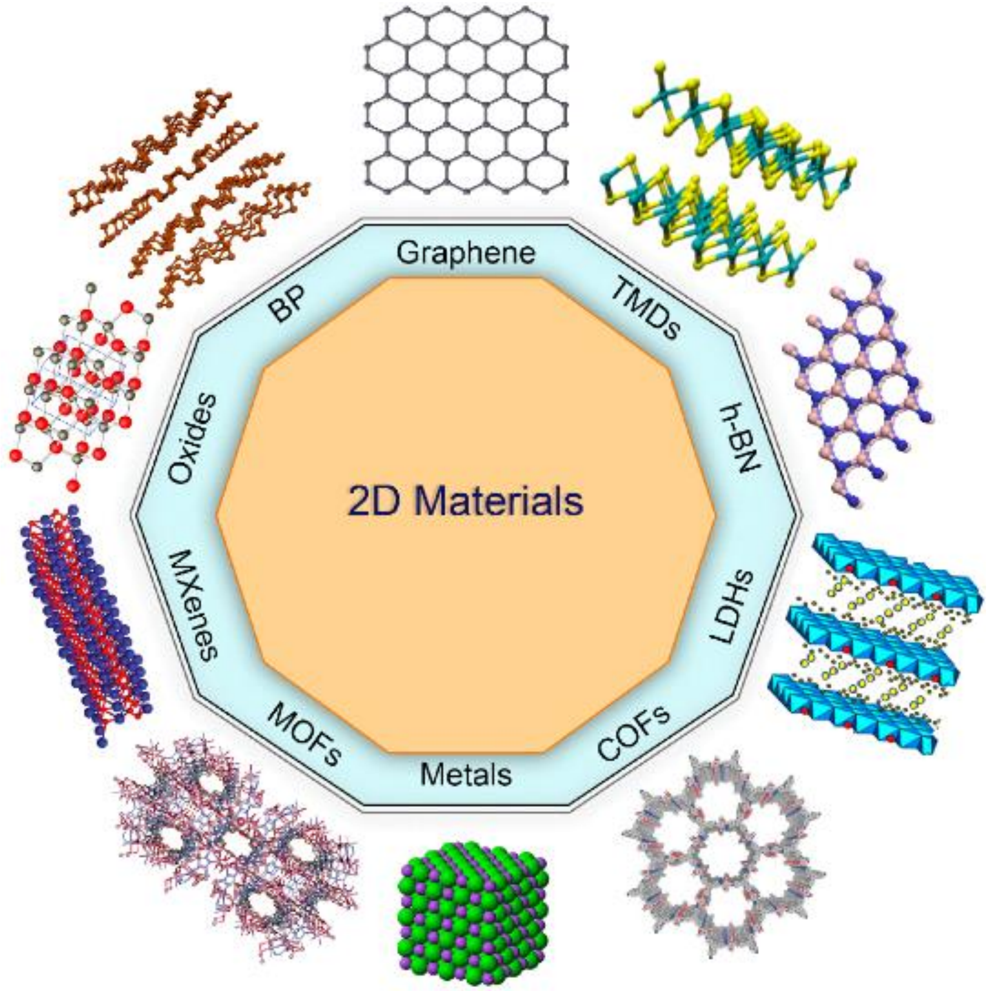

Figure 1.1 Schematic diagram to introduce 2D material family. Image from(*2*)

1.1.1 Indium selenide

In_2Se_3 is a two-dimensional layered material, a representative member of the III-VI material family, where each layer is connected by strong covalent bonds in a Se-In-Se-In-Se configuration, while the interlayer interaction is governed by weak van der Waals forces. It exhibits complex polymorphism and possesses five stable phases (α, β, γ, δ, and κ) with different stoichiometric (InSe, In_2Se_3, In_3Se_4)(*3, 25*). Understanding the phase transitions between these phases and elucidating the underlying mechanisms is crucial for harnessing the full potential of indium selenide family. Exceptional ferroelectricity, and antiferroelectricity observed in few-layer α-In_2Se_3 and have β'-In_2Se_3 attracted researchers to explore its ability in overcoming traditional limitations in silicon logic gates, leading to a novel ferroelectric semiconductor field-effect transistor (Fes-FET) with a high 10^8on/off ratio(*26*).

The paper presents exceptional plasticity and deformability observed in bulk single-crystalline indium selenide β-InSe(*4*). The study shows that InSe crystals can undergo significant compression, folding, bending, winding, and morphing at room temperature without breaking, which sets it apart from other similar 2D materials and semiconductors. Through transmission electron microscopy and in-situ compression experiments, researchers identified the deformation mechanisms involving interlayer gliding and cross-layer dislocation slip along slip planes like (10L). Density functional theory calculations revealed that the intralayer In-Se bonding in InSe contributes to its low intralayer modulus and pliability, while the interlayer interaction involves a long-range Coulombic interaction between In and Se atoms across layers, providing sufficient interlayer integrity for plastic deformation via gliding and slip.

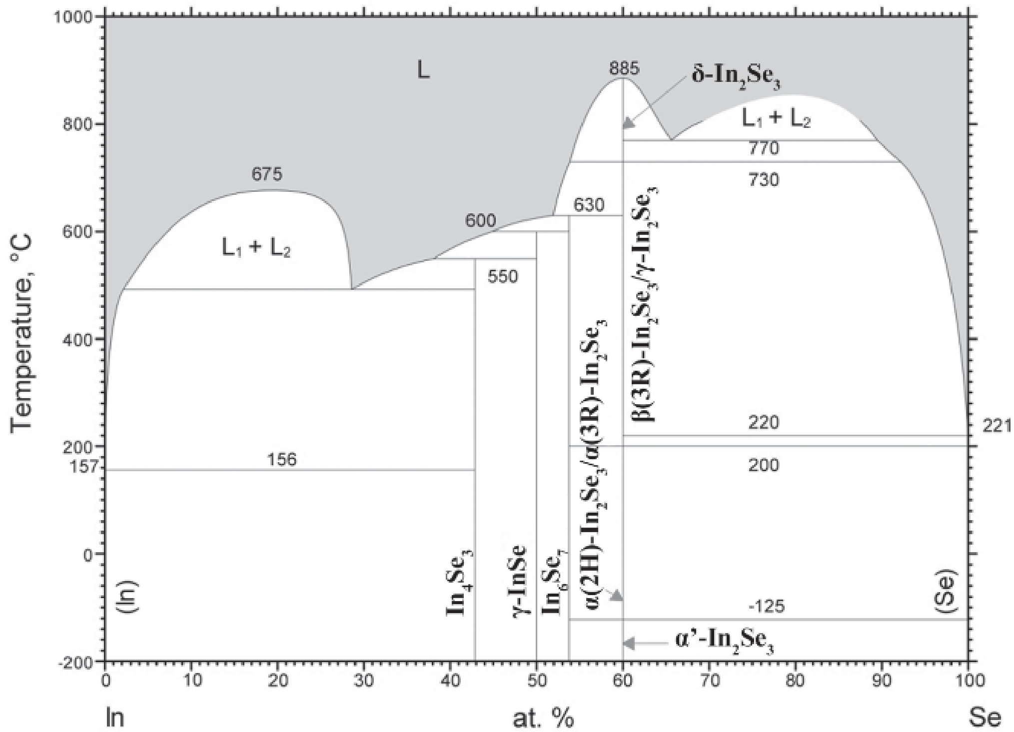

Figure 1.2 In-Se binary phase diagram showing polymorphism of indium (III) selenide. Image from (*3*)

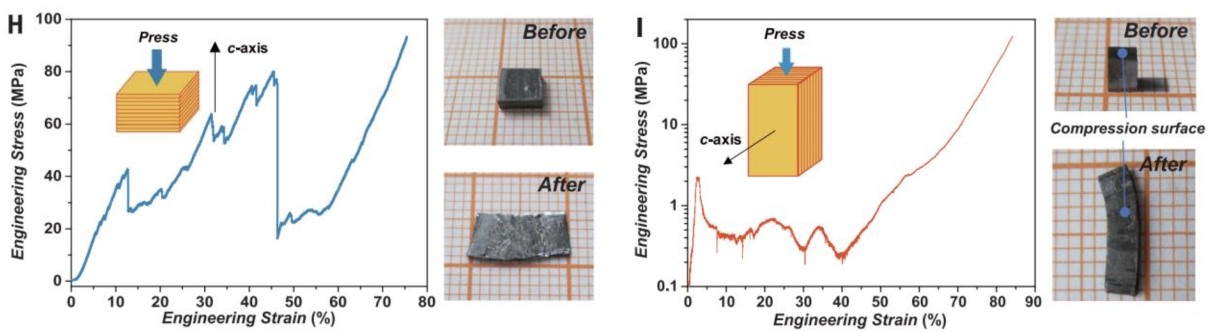

Figure 1.3 Exceptional plasticity in the bulk single crystalline InSe. Image from(*4*)

1.1.2 Transition metal Dichalcogenides (TMD)

Transition metal dichalcogenides (TMDs) have garnered significant attention in research due to their tunable bandgap, direct electron transitions in monolayers, and high mobility in devices. The success of graphene fabrication and applications has prompted investigations into

2D materials exhibiting semiconductor properties. Unlike graphene, which lacks a bandgap in its electronic structure (owing to the presence of a Dirac cone), TMDs offer the potential for rectifying electric current and effectively turning off with minimal leakage current. The layered structure of TMDs overcomes the limitations of semimetallic graphene. Typically, TMDs consist of a transition metal element (such as Mo or W) and a dichalcogenide element (e.g., S or Se), forming a triple atomic layer in a single-layer structure. This structure exhibits an intrinsic layer arrangement denoted as [X-M-X], where the transition metal layer is sandwiched between dichalcogenide layers through strong intralayer covalent bonds and weak interlayer van der Waals forces. Figure 1.4 illustrates the structure of TMDs.

Taking the electronic band structure of MoS_2 as an example, the wavevector values corresponding to the top of the valence band and the bottom of the conduction band in the bulk phase band structure are different, indicating a difference in momentum between electron transition, which is a common characteristic of transition metal dichalcogenides (TMDs). In the case of a single-layer MoS_2, the bandgap measures 1.8 eV,(*27*) and the valence band maximum and conduction band minimum align at the K point. This contrasts with the bulk MoS_2, where the bandgap is reduced to 1.3 eV. Different conditions, such as the 1T phase, can induce phase transitions in MoS_2, leading to semi metallic properties. Notably, this phase transition holds promise as a potential solution for mitigating the high interface resistance associated with silicon Schottky contacts in two-dimensional semiconductors and metals(*28*).

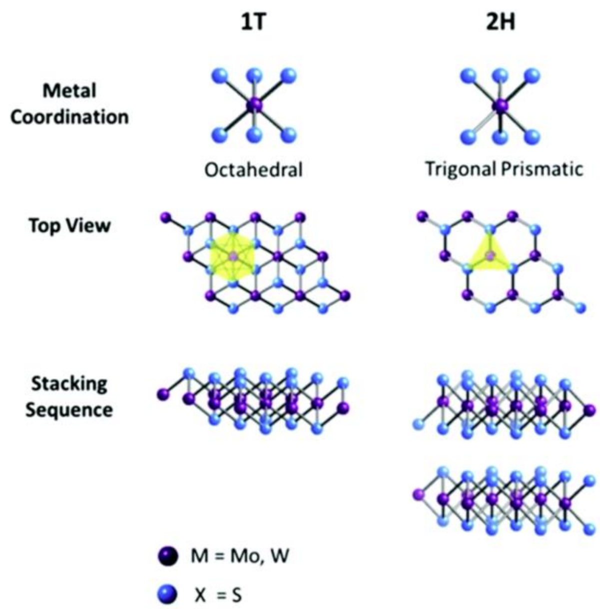

Figure 1.4 Illustrate the atomic structure of TMD. Image from(*5*).

1.1.3 Rationale for Material Selection and Objectives

Our research has selected 2D materials such as In_2Se_3, MoS_2, and WS_2 due to their semiconducting and exceptional properties that make them stand out as possible alternatives to silicon(*29, 30*). In_2Se_3 is of particular interest for its ferroelectric capabilities and phase-change characteristics, which are important in non-volatile memory applications(*26, 31*). MoS_2 and WS_2 offers high electron mobility and stability, making it suitable for flexible and wearable electronics, which is essential for electronic devices(*32, 33*). These unique properties and potential applications are the driving force behind their selection for our study.

The primary objective of our study is to explore the synthesis methods for these 2D materials and to establish heterostructures. We aim to investigate their growth morphology about experimental growth parameters and to enhance the atomic structure of the junctions. Additionally, we plan to delve into the phase controllability of In_2Se_3 using the CVD method and respond to environmental stimuli such as bending and thermal expansion. The phases within

In_2Se_3 are complex. Much of the research on this material has yielded contradictory results. These discrepancies are likely due to the presence of mixed phases within the specimen(*34, 35*). Therefore, it is important to study direct synthesis methods that can yield high-quality In2Se3 with controllable phases. Furthermore, the heterostructure junction is the core of electronic device architecture, playing a critical role in dictating the performance of the device. These junctions, which serve as the interface between dissimilar materials, are engineered to modulate properties such as charge accumulation, potential barriers, and electronic band alignment. Consequently, the careful design and optimization of heterostructure junctions are essential to enhance device functionality.

This study is designed to offer significant insights into the field of two-dimensional materials, with a focus on $In2Se_3$, MoS_2, and WS_2. By conducting synthesis and a detailed atomic structure analysis of junctions and exercising precise phase control, we aim to deepen our understanding of the synergistic effects and growth of heterostructures. Our research is meant to contribute to the development of advanced materials and next-generation semiconductor technologies.

1.2 Preparation of Two-dimensional material

Numerous techniques have been investigated for the fabrication of thin film deposition of 2D materials across different classes. These techniques include mechanical and liquid exfoliation of bulk single crystals, chemical vapor deposition (CVD), and molecular beam epitaxy. , the key methods employed in the preparation of large amount and high-quality of 2D material present notable challenges.

1.2.1 Mechanical Exfoliation

Mechanical exfoliation techniques as shown in Figure 1.5, specifically micromechanical cleavage using Scotch tape, provide a straightforward approach to obtain graphene flakes. However, these techniques have limitations concerning scalability, controllability in the thickness of the flakes, and the complexity involved in removing residual substances. In micromechanical cleavage, Scotch tape is applied to the graphite surface, generating a normal force that overcomes the van der Waals attraction between adjacent graphene layer. Through repeated iterations, the graphitic layer progressively becomes thinner until it reaches a single-layer graphene state. While this method can yield high-quality and large-area graphene flakes, it is labor-intensive, time-consuming, and not suitable for industrial-scale production(*6*).

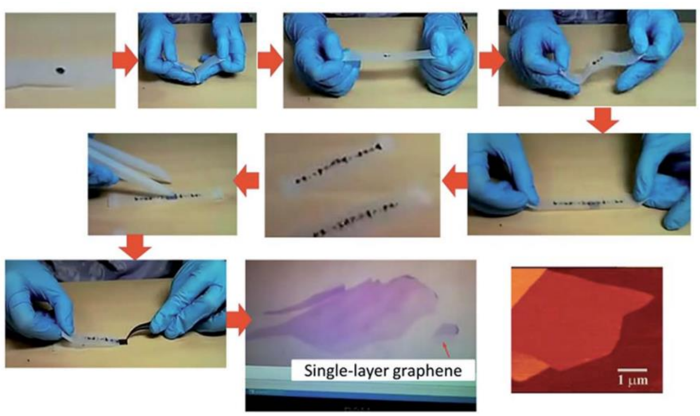

Figure 1.5 Illustrate mechanical exfoliation for the scalable production of graphene. Image form(*6*)

1.2.2 Liquid-Phase Exfoliation

Chemical exfoliation techniques, including liquid-phase exfoliation and ion-intercalation-induced exfoliation, provide effective methods for separating monolayer or few-layer 2D sheets from bulk materials in large quantities. In liquid-phase exfoliation, a polar solvent is used to immerse the material, leading to expanded van der Waals separation between the 2D layers at the interlayer junctions. Through sonication, the bulk material is fragmented into individual platelets, which can then be further separated into monolayers or few-layer sheets using centrifugation. To achieve stable suspension, a suitable solvent with sufficient surface energy is chosen to overcome the van der Waals interactions between the interlayers of the bulk material. This method has been successfully applied to various layered compounds such as MoS_2, WS_2, $MoSe_2$, $MoTe_2$, $TaSe_2$, $NbSe_2$, $NiTe_2$, h-BN, and Bi_2Te_3(*8*). These compounds can be efficiently dispersed in common solvents and deposited as individual flakes or formed into films. In comparison, the liquid-phase exfoliation method offers advantages such as high processability, low cost, short preparation cycles, and the potential for large-scale production. However, it is worth noting that the resulting flakes may exhibit variations in lateral size and thickness, which may not be ideal for wafer-scale fabrication in the silicon industry.

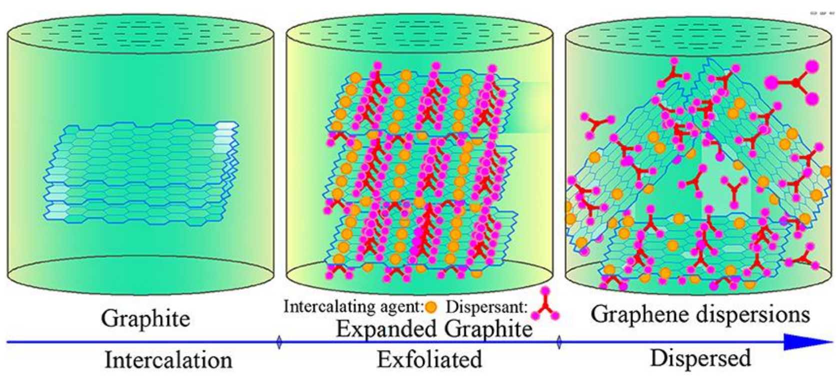

Figure 1.6 Stripping graphite in liquid phase. Image from (*7*).

Figure 1.7 Massive production of nano flake of 2D material with liquid exfoliation. Image from (*8*)

1.2.3 Chemical Vapor deposition

The size and quality of solution-prepared and mechanical exfoliated 2D materials are critical considerations in hindering various applications. In this regard, gas-phase-based direct growth methods, particularly chemical vapor deposition (CVD), offer a scalable and controllable approach to synthesizing large-area, high-quality 2D materials at reasonable costs. These advantages make CVD highly significant for research and explorations in the realm of 2D materials. Researchers have discovered various correlations between the parameters employed in CVD and the resulting 2D materials produced, detailed discussed in the review(*9*). For short, CVD typically involves the reaction of gaseous precursors evaporated from solid oxide either in the gas phase of organic molecular or pre-deposited metal film on the surface of a substrate, applying high thermal condition to lead to the reaction occurring at the substrate surface. The number of layers, their size, morphology, orientation, as well as the introduction of dopants or defects, can be controlled by manipulating growth parameters such as temperature, chamber pressure, gas flow rate, relative amounts of source materials, and source-to-substrate distance. The progress in CVD techniques and the growth of 2D materials can collectively contribute to the rapid advancement of 2D material research since the discovery of graphene. With the emergence of large-scale and high-quality CVD-grown samples speed up their widespread application of 2D nano-film.

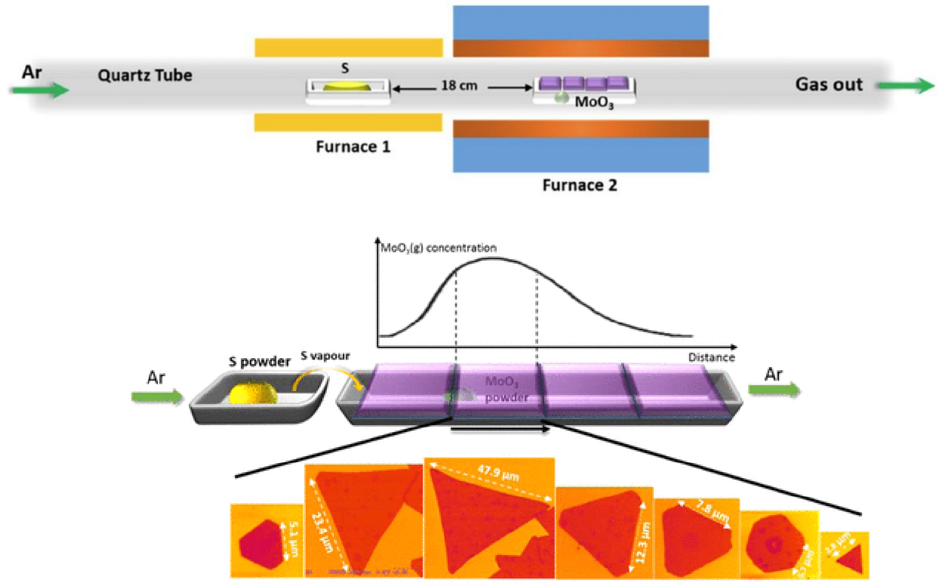

Figure 1.8 Schematic diagram of a CVD tube furnace and growth of MoS_2 in different gasses concentrations due to supply distance. Images from (*9*)

Taking the growth of In_2Se_3 as an example, common precursors such as In_2O_3 and Se are utilized. The reaction involves the formation of volatile sub-oxide species, $In_2O_{3-x}Se_x$, which arise from the partial reduction of In_2O_3 by selenium vapor in the precursor. These sub-oxide species are then transported and carried by a mixture of hydrogen and nitrogen gases. Upon reaching the mica surface, these reactants are absorbed and undergo continuous selenization, resulting in the formation of a covering of In_2Se_3. The reaction can be represented by the following simplified equation(*31*):

In precursor: $In_2O_3 + x\ Se + x\ H_2 \rightarrow In_2O_{3-x}Se_x + x\ H_2O$

On surface of mica: $In_2O_{3-x}Se_x + H_2 + (3-x)\ Se \rightarrow In_2Se_3 + H_2O$

With the presence of InSe powder mixed with In_2O_3, the overall reaction can be modified to favor the formation of reactive species in the precursor, specifically $InSe_{1+y}$.This modification leads to the dynamic formation of Se-defective In_2Se_3, which corresponds to the β' phase after cooling down of synthesis. Density functional theory (DFT) calculations confirm the ground-state energies of the monolayer β' phase with Se vacancies is found to be more stable than the Beta phase(*31*).

1.2.4 Molecular beam epitaxy

Molecular Beam Epitaxy (MBE) is an advanced thin film growth technique that operates within an ultra-high vacuum environment. This method employs the co-deposition or shuttered growth of molecular beams(*10*). The process commences by heating the source material in an effusion cell, which is subsequently ejected into an ultrahigh vacuum reaction chamber with the assistance of plasma and ozone. The atoms comprising the molecular beam are then adsorbed onto the substrate surface, referred to as adatoms, initiating an interaction between these adatoms and the surface. Over time, the surface progressively accumulates the desired elements, resulting in the formation of films on the substrate. MBE is recognized for its exceptional capacity to produce films of the utmost quality while precisely controlling their atomic layers. Consequently, MBE has found substantial success in facilitating the growth of diverse material systems.

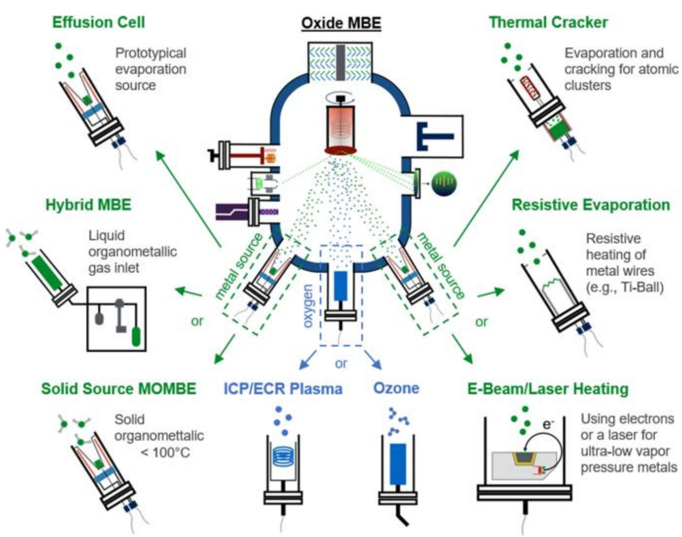

Figure 1.9 Schematic diagram of MBE system offer versatility in the choice of source materials and deposition method. Images from(*10*).

1.2.5 Summary of synthetic Method

A comparison of these methods is presented in Table 1. CVD demonstrates the highest potential for producing large-scale, high-quality 2D material with controlled layer numbers at a relatively low cost(*9, 36*). Consequently, CVD has become the most widely employed method for 2D material synthesis. In this study, we will mainly focus on the use of CVD to synthesize single-crystalline of In_2Se_3, MoS_2, WS_2, and their hetrostrucutre. Selecting CVD as primary growth provides some advantages. In terms of strain management, the setup of CVD equipment allows for control over the cooling rate, which is useful in managing thermal-induced strain effects(*37, 38*). The design of a sophisticated CVD system can facilitate the movement of the heating zone with sliding tube design that enables rapid cooling rates when necessary. Additionally, the use of liquid nitrogen and various cooling methods, such as soaking in coolant, tuning gas flow, or air cooling by opening the furnace at specific times, provides an alternative to control cooling rates. These methods are crucial in achieving different strain profiles in the final material. For instance, a slower cooling rate often results in lower defect densities and higher-quality crystals, as it allows for a more gradual relaxation of thermal stress(*9*). In contrast, the strain conditions of crystals produced by mechanical exfoliation is dependent on the manual transfer process, the quality of the parent bulk material, and the exfoliation method. While exfoliation may yield materials in an equilibrium state with fewer strain management concerns, it lacks the level of control found in CVD processes. Compared to MBE, which is another sophisticated thin-film deposition technique, CVD offers some advantages. MBE typically operates at lower temperatures, which can limit the lateral size of the films and result in a higher density of grain boundaries. These grain boundaries can influence mechanical properties, such as work hardening in bulk materials(*39*), which may obscure the intrinsic properties of the 2D material. CVD, with its higher growth temperatures and ability to produce larger-area films, can help to minimize these effects of grain defects (*40, 41*).

Lattice mismatch refers to lattice constants between a target material being grown (the film) and the substrate or host material. When the lattice constants of the film and the substrate differ significantly, growth can be challenging due to the induced strain. This strain can manifest as various defects, such as dislocations, misfit dislocations, and planar defects within the material. For example, in the growth of gallium nitride on sapphire, an aluminum nitride buffer layer is often employed. The AlN buffer layer serves to better accommodate the lattice mismatch between the GaN and the sapphire substrate, helping to mitigate the strain and associated defects(*42, 43*).Lattice mismatch helps assess the likely strain and potential for defect formation during the growth process. In 2D materials, such as graphene and TMDs, lattice mismatch can be less detrimental than in 3D materials. This is because 2D materials are bonded by van der Waals forces, which are relatively weak compared to the covalent or ionic bonds found in 3D materials. As a result, 2D materials can accommodate lattice mismatches more easily, allowing for the growth of heterostructures with less concern for excessive strain and without the strict lattice matching requirements commonly necessary for 3D epitaxial growth(*11*).

vdW epitaxy differs from traditional epitaxial methods in terms of the requirement of lattice match between the film and the substrate. Instead, it utilizes the weak van der Waals interactions between the 2D material and the vdW-compatible substrate. This growth mitigates strain and minimizes the formation of defects, allowing 2D materials to be grown on a broad array of substrates, even those with lattice constants that differ significantly. Particularly, it is beneficial for the integration of 2D materials into existing device architectures. The weak vdW force enable stacking and crafting of vertical heterostructures, composed of various 2D materials.

Such structures can be engineered to possess customized properties and specific technological applications(*44*). For example, the growth of MoSe2 on HOPG have 33% lattice mismatch but with no strain phenomena observed(*45*).

Table 1 A comparison of various methods for the 2D material synthesis

	Mechanical Exfoliation	Liquid-Phase Exfoliation	Chemical Vapor deposition	Molecular beam epitaxy
Advantages	Simple and cost-effective	Productive method	Precise control in film thickness, uniformity, and composition.	Provides atomic layer control and precise control over film thickness
	High-quality	High exfoliation efficiency	High deposition rates	the growth of films with exceptional quality and purity
	Allow artificial stacking		high-quality films with excellent crystalline structure	Facilitates the formation of heterostructures with precise control interfaces
Disadvantages	Labor-intensive	Low quality with random thickness	Limited availability of precursor	Requires an ultra-high vacuum environment and complex equipment.
	Limited scalability	Contamination to product	Requires complex equipment and high-temperature conditions	Low deposition rates and limited scalability for large-scale production
	Low yield	Introduce defect		Expansive
	Uncontrollable in thickness			

1.3 Growth mechanisms of CVD

In the section focusing on the fundamental nucleation and growth mechanism of 2D materials using the chemical vapor deposition (CVD) technique, we delve into the topic of epitaxial growth of materials.

1.3.1 Conventional and Van der Waals epitaxies

A material is grown epitaxially on a substrate with a different lattice constant. The strain will occur if there are no strain-relieving extended defects like dislocations. The interfaces between the layer and substrate are continuous in the absence of such defects. The strain is compressive when the layer has a larger lattice constant than the substrate, and vice versa. People discuss the strain with lattice mismatch as the equation(*46*),

$$strain = \frac{a_{substrate-a_{film}}}{a_{substrate}}$$

The strain energy stored at the interface depends on the lattice parameter difference, and defect density. Plastic deformation can occur when the strain energy is significant, leading to the introduction of misfit dislocations that reduce stress.

2D materials lack surface dangling bonds and interlayers are connected by van der Waals force. In contrast to conventional epitaxy, where atomic covalent or ionic bonding is formed on a surface, certain cases of epitaxial growth of 2D materials occur through van der Waals forces. This type of epitaxy, known as van der Waals epitaxy, allows for growth on substrates with significant lattice mismatches. As a result, it enables the creation of heterostructures with atomic-level thickness. As depicted in Figure 1.10.

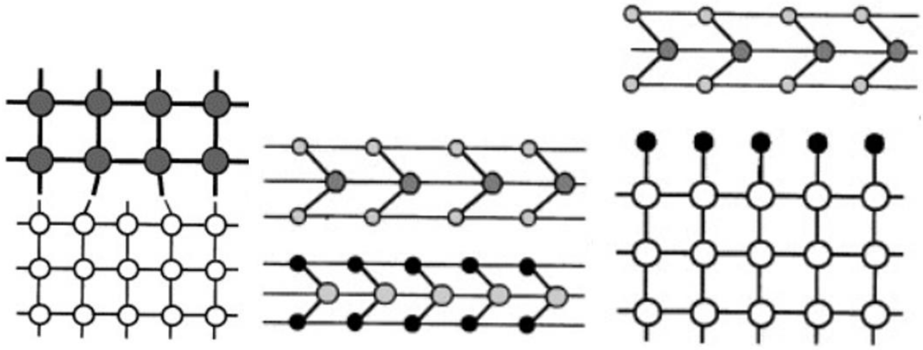

Figure 1.10 Epitaxial growth of layer with strain, and interfacial misfit dislocations. Image from(*11*).

1.3.2 Nucleation and surface absorption

During the film growth step, atoms or molecules from the gas phase adsorb onto the substrate surface. These adsorbed species undergo surface diffusion and slightly attract with the substrate atoms through bonding mechanisms such as chemical bonding or van der Waals forces. They move across the substrate's surface to find energetically favorable positions. As more atoms or molecules continue to adsorb and aggregate as small nuclei. The growth of the film involves the coalescence of these nuclei, leading to the formation of a continuous and coherent film on the substrate surface.

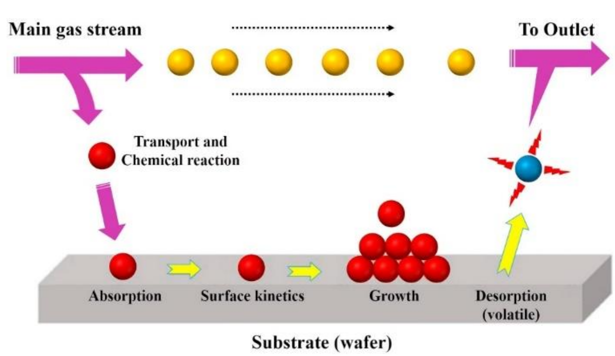

Figure 1.11 Schematic of deposition process on the substrate and surface processes in CVD. Image from (*12*)

1.3.3 epitaxies growth modes

Researchers classify growth modes into three fundamental types, allowing for deeper comprehension and control of thin film growth mechanisms. These types encompass the layer-by-layer growth mode (also known as Franck-van der Merwe), the island growth mode (or Vollmer-Weber), and the layer plus island growth mode (referred to as Stranski-Krastanov).

(i)In the layer-by-layer growth mode, the growth of a new layer begins only after the preceding layer has completed its formation. This mode implies a sequential layer-by-layer growth process.

(ii)The layer plus island growth mode represents an intermediate case between the layer-by-layer and island growth modes. Initially, one or a few monolayers form in a layer-by-layer manner. However, as subsequent layer growth becomes unfavorable, islands start to form on top of the layers.

(iii)The island growth mode occurs when small clusters, or islands, are nucleated on the substrate surface. This mode arises when the atoms or molecules forming the film have stronger bonds with each other compared to their interaction with the substrate.

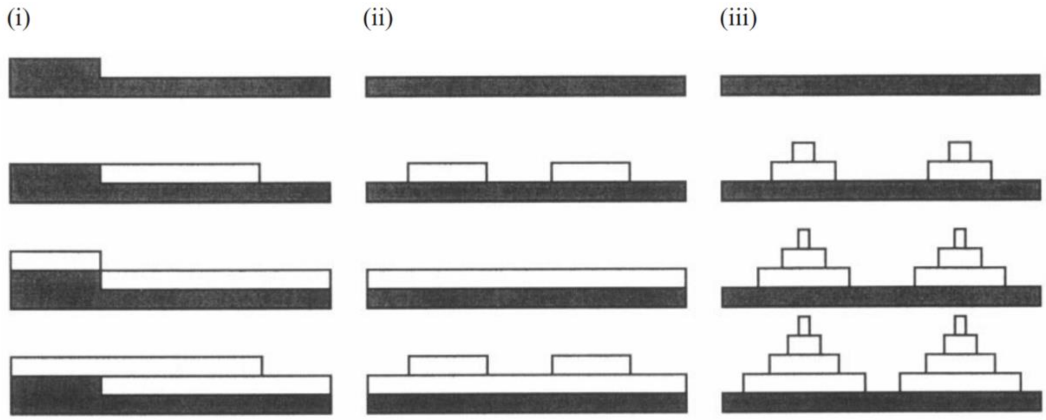

Figure 1.12 Cross-section views of the three primary modes of thin-film growth(*13*)

1.4 Importance of Phase Controllability in Ferroelectric Materials

Ferroelectric materials are characterized by their unique property of spontaneous polarization, resulting from an inherent asymmetry in the unit cell structure. This polarization emerges without external electric fields, leading to permanent dipoles within the material. These materials exhibit responses such as the piezoelectric effect when stressed or switching of the internal polarization state when an external electric field is applied. This makes them attractive for enhancing the functionality and performance of various devices, including memory storage, sensors, transistors, and photovoltaic cells.

1.4.1 Traditional Ferroelectric Materials

The concept of molecules carrying a permanent dipole moment below a certain critical temperature, is now known as the Curie temperature. In the history of ferroelectric materials was the discovery of ferroelectricity in rochelle salt ($NaKC_4H_4O_6 \cdot 4H_2O$) by Joseph Valasek in 1921 (*14*). Despite its complex crystal structure, ferroelectric properties of rochelle salt were groundbreaking, leading to its first application in electromechanical transducers and sensors. The ferroelectric behavior is the first recorded hysteresis loop provided a deeper understanding of these materials(Figure 1.13).Following this, the discovery of ferroelectricity in potassium dihydrogen phosphate (KH_2PO_4) by Busch and Scherrer in 1935 further expanded the understanding of ferroelectric materials(*47*). The breakthrough came with the simplicity of oxide perovskite structures, it was the synthesis of barium titanate (BaTiO3) in 1941 that truly revolutionized the field. As the first human-made ferroelectric oxide metal, barium titanate was utilized during World War II to create ceramic materials with superior dielectric permittivity compared to other ceramics known at the time. Its primary use in multilayer ceramic capacitors marked the beginning of ferroelectric materials in electronic applications(*48*). The subsequent development of lead zirconate titanate (PZT) in 1952 further underscored the importance of ferroelectric materials in the industry, leading to the creation of numerous useful devices.

However, traditional bulk ferroelectric materials face challenges with the trend toward miniaturization in the semiconductor industry. As these materials are thinned down to accommodate smaller device sizes, they often exhibit instability. It poses significant integration hurdles for contemporary nanoscale electronics.

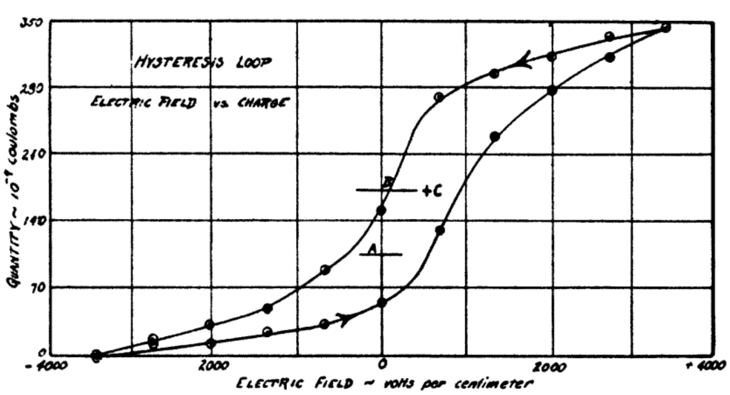

Figure 1.13 the hysteresis loop of Rochelle salt. Image from (*14*)

1.4.2 2D Ferroelectric Materials

Two-dimensional (2D) materials have shown remarkable stability in maintaining ferroelectric properties even at atomic-level thicknesses. Our research is focused at In_2Se_3, which have stable ferroelectricity even when approaching to monolayer thickness and at room temperature. Generally, III-VI group materials can have different stoichiometries, such as InSe, In_2S_3, In_2Se_3, and In_3Se_4. III-VI family of Indium – selenium has a more complex set of polymorphs provide them with a wide range of physical and chemical properties(*3*). Among In_2Se_3, there are eight different phases of α, α', β, β', γ, γ', δ, and κ (Figure 1.14). The thesis is focused on the α and β' phases, which have layered structures. The structural characteristics of these phases and the transitions between them are largely unclear or even contradictory in the literature. For example, layer thickness-dependent transition temperature between α and β phases(*49*), formation of intermediate β' phase(*50*), and α- β' phase transition dependent on cooling rate(*37*).

Previous studies on In_2Se_3 have shown contradictions due to structural complexities. The synthesis of high-quality In_2Se_3 single crystals and precise phase control has thus become an important task. Crucially, the ferroelectric properties of In_2Se_3 primarily stem from phase transitions or the presence of mixed phases within the material. α-In_2Se_3 exhibits out-of-plane ferroelectricity, while β'-In_2Se_3 shows in-plane antiferroelectricity.

The different ferroelectric states are dependent on the phases, with both in-plane and out-of-plane ferroelectricity observed due to the presence of mixed phases. Therefore, research into controlling the phases of In_2Se_3 is of great importance and significance. This control helps in electronic device applications. The distinct phases present the possibility of manipulating ferroelectric and antiferroelectric properties, as well as transitioning between out-of-plane and in-plane properties. These phase controls may help to realize the heterostructure that is phase switchable.

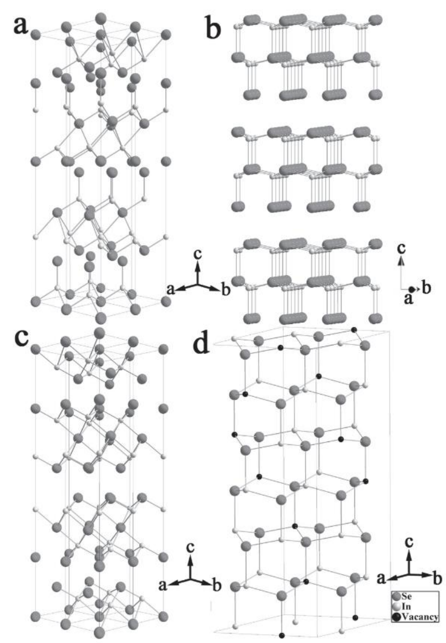

Figure 1.14 atomic model of In_2Se_3 (a)α(3R), (b)α(2H), (c) β(3R) and (d) γ. Image from (*3*)

1.5 Potential Applications in Advanced Electronic Devices

In 2D vdW materials, ferroelectricity offers a wide array of applications. In the work demonstrated by Wang, they have fabricated a $CuInP_2S_6$ as shown in Figure 1.15. The ferroelectric transistor memory cell has developed offers long retention exceeding 10 years and displays impressive operational characteristics of 17 mV dec^{-1}, a memory window that exceeds 3.8 V, and a programming/erasing ratio greater than 10^7. Additionally, the device demonstrates exceptional durability over 10^4 cycles, and high programming/erasing speeds below 5 μs. The superior performance positions device architecture as a suitable candidate for non-volatile memory applications and suggests that vdW engineering is a practical solution to the challenges of ferroelectric memory retention.

In other work, the group of Dagdeviren presents a PZT sensor designed for integration into biological devices, see the Figure 1.16. This sensor is specifically engineered to measure blood flow pressure changes with high sensitivity (~ 0.005 Pa) and a rapid response time (~0.1 ms). The flexibility of PZT sensor makes it particularly valuable for continuous health and wellness monitoring in a clinical setting. The potential applications of this sensor are extensive, ranging from the detection of vital signs to the early identification of cardiovascular events, as well as the ongoing assessment of an individual's health status.(*16*)

In the field of photovoltaic, Yue Li has reported a bulk photovoltaic effect in the ferroelectric material $CuInP_2S_6$ (Figure 1.17), which exhibits a photocurrent density that is two orders of magnitude greater than that of traditional bulk ferroelectric perovskite oxides. The thin-film $CuInP_2S_6$ facilitates the capture of photovoltaic energy without the need for p-n junctions or external bias. Despite the substantially reduced thickness of $CuInP_2S_6$ compared to traditional bulk ferroelectric perovskites, its photoconductivity is comparable to that of other materials. This discovery paves the way for the application of two-dimensional ferroelectrics in photovoltaic devices, potentially advancing the field of solar energy conversion.

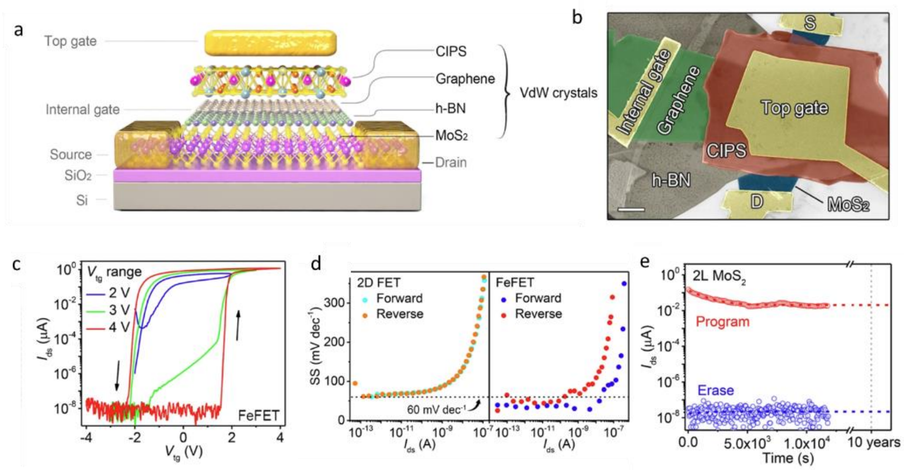

Figure 1.15 (a) Schematic diagram of an MoS_2/h-BN/graphene/ $CuInP_2S_6$ vdW FeFET. (b)False-color SEM image of a typical vdW FeFET. (c)electric characteristics of the device at various gate voltage ranges measured with $V_{ds} = 0.5$ V and internal gate floating. (d)SS−Ids characteristics. (e)Program and erase state retention properties of the device. Image from (*15*)

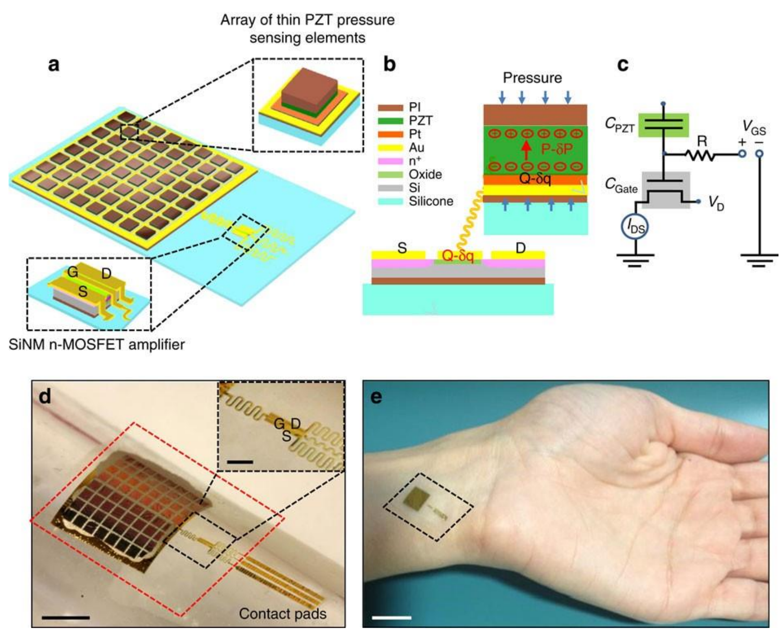

Figure 1.16 (a)Illustration of the PZT sensor. (b)Cross-sectional view of the schematic of the pressure sensor with its electronic component connection. (c)Equivalent circuit. (d) optical image of a device wrapped on a cylindrical glass support. (e) Photograph of daily application for the device. Images from(*16*)

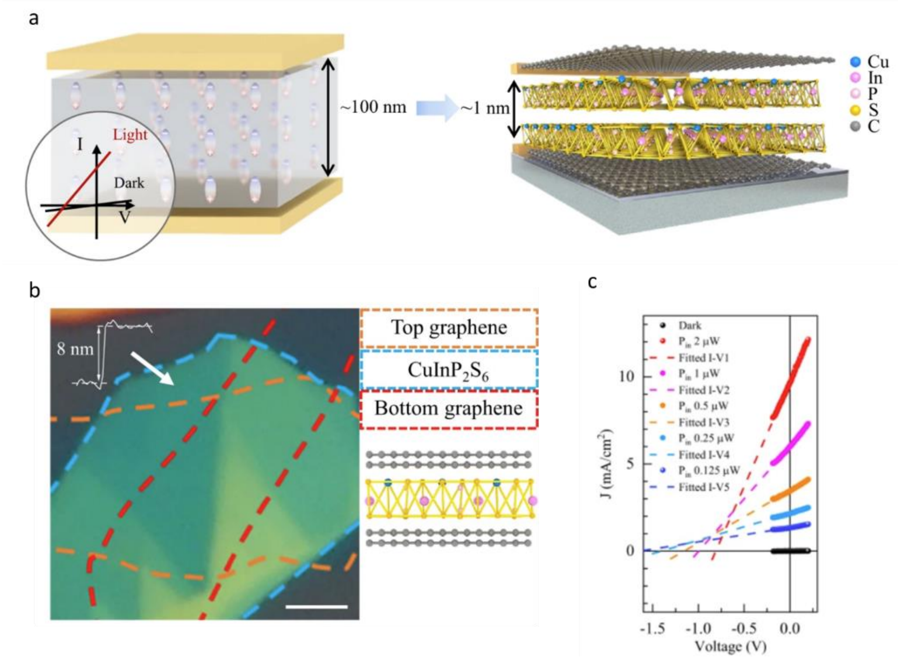

Figure 1.17 (a) The schematic structure of 3D and 2D photovoltaic effect device. (b) optical image of the device. (c) The characteristic output I–V curves of device measured at bright conditions with different laser power. Image from

1.6 Structure of thesis

Section 1 is the introduction. we provide a comprehensive overview of 2D materials, their synthesis processes, and synthesis techniques. We begin with a general review of the growth mechanisms and models employed in the synthesis process of 2D materials. We also introduce the specific material of interest and provide an overview of the samples (In_2Se_3, MoS_2, WS_2) that will be investigated in subsequent chapters.

Section 2 is the methodology of synthesis and characterization. This section delves into the methodology employed for the synthesis and characterization of the mentioned materials. We employ chemical vapor deposition as the primary synthesis technique, which enables the production of a diverse range of high-quality materials. Additionally, we discuss the transfer techniques utilized to manipulate and handle the synthesized materials. The characterization of the materials is carried out using advanced equipment specifically chosen for this purpose.

In Section 3, we present the synthesis protocol for atmospheric CVD, providing a detailed derivation and analysis of the CVD process and its associated parameters. We investigate the influence of various factors such as substrate choice, reaction duration, quantity, and substrate-source distance on the synthesis of In_2Se_3. Furthermore, we focus on the manipulation of the phase and lateral size of the synthesized materials, emphasizing their significance.

Section 4 is dedicated to the synthesis protocol of the MoS_2-WS_2 heterostructure. We employ aberration-corrected scanning transmission electron microscopy (STEM) as a powerful tool to investigate the structural and electronic properties of the heterostructure. We discuss the selection of growth conditions, and intricacies of the experimental setup for achieved heterostructure.

In the final section, we summarize the findings and observations related to the heterostructures of $\mathbf{In_2Se_3}$ and MoS_2-WS_2. We discuss the significance of interface engineering in these heterostructures and outline future research directions to further advance our understanding and optimize their properties.

Chapter 2. Methodology

2.1 experimental chemical

The main materials and reagents used in this study are listed in Table 2. All materials and reagents were used as received without any additional treatment prior to use.

Table 2 Essential experimental materials and reagents

Material and Regent	Chemical formula	Purity	Purchase source
Indium (III) Selenide	In_2Se_3	99.99%	Innochem
Molybdenum trioxide	MoO_3	99%	Innochem
Tungsten trioxide	WO_3	99.99%	Aladdin
Sulfur Powder	S	99.998%	Sigma-aldrich
Selenium Powder	Se	99.99%	Aladdin
Sodium Chloride	NaCl	99.5%	Aladdin
Potassium Hydroxide	KOH	ca. 85%	Acros Organics
Acetone	CH_3COCH_3	99.5%	Anaqua
Ethanol	CH_3CH_2OH	99.9%	Anaqua
Fluorophlogopite Mica	$KMg_3(AlSi_3O_{10})F_2$	-	-

2.2 Process flow of CVD synthesis

The schematic diagram of the CVD system used in this study is shown in Figure 2.1. The system includes a tube furnace, specifically the LFT1200C model with double temperature zones, manufactured by CPI Company (康帕因). The furnace is equipped with a quartz tube that is 1 meters long and has a diameter of 1 inch (. The maximum heating temperature of the tube furnace is 1200°C. In this study, various substrates are used for synthesis.

The reaction temperature is controlled by the heating center of the tube furnace of each heating zone, while one is for heating metal source and another for dichalcogenide. On the right side of the system, there are two gas inlets for 5% hydrogen mixed with 95% nitrogen and pure argon, respectively. The gas flow rates are controlled by gas mass flow controllers, with a range of 0-500 sccm (standard cubic centimeters per minute). On the left side of the system, there is an exhaust outlet through which the exhaust gas is treated and released into the atmosphere by the exhaust gas treatment system. The entire system operates at atmospheric pressure.

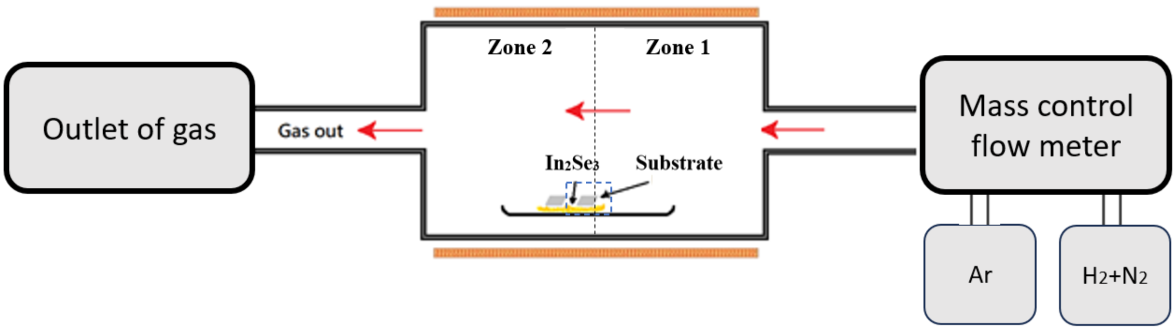

Figure 2.1 Schematic of diagram of CVD system

The process flow for sample preparation using the CVD method is as follows:

Step 1: Substrate Preparation

The silicon wafer (300 nm-SiO_2/Si)/sapphire/ pure silicon is first cut into substrates with dimensions of 1 cm x 1 cm. The substrates are then sequentially cleaned in acetone and isopropyl alcohol using ultrasonic cleaning for 15 minutes. Subsequently, they are cleaned with deionized water and dried with nitrogen gas. In other cases, the mica, and HOPG are cleavaged by sharp blade and scope tape respectively.

Step 2: Loading and Weighing of Reaction Sources

Taking the preparation of In_2Se_3 as an example, 65 g of In_2Se_3 powder is accurately weighed using an electronic balance. The powders are thoroughly mixed and placed in a quartz boat. Then, the substrates are inverted and placed on top of the quartz boat, with the front side facing downwards.

Step 3: Cleaning of the CVD System

After the reaction sources are properly p tube furnaces are purged by high-purity gas at a flow rate of 300~500 sccm for 10 minutes.

Step 4: Reaction

Once the setup is complete, the experimental parameters are set according to the requirements, and the reaction is initiated. The typical temperature-time curve for the CVD method, which shows the relationship between reaction temperature and time, is illustrated in Figure 2.2.

The entire reaction process can be divided into three stages: heating (I), isothermal reaction(ii), and cooling(iii). During the heating stage, the system is heated from room temperature, causing the precursor reaction sources to evaporate. In the reaction stage, the vaporized source materials undergo chemical reactions and nucleate and grow on the substrate surface. Finally, in the cooling stage, the system naturally cools down to room temperature.

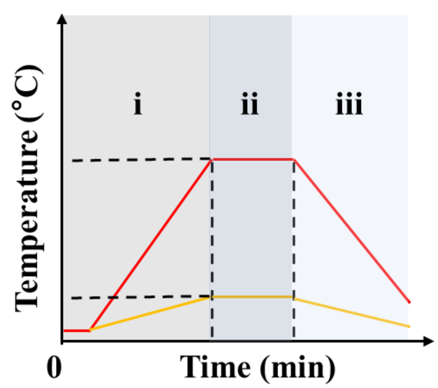

Figure 2.2 CVD temperature vary time diagram.

2.3 Wet-transfer methods

The as-grown samples obtained on mica, SiO_2/Si or others substrates were transferred to TEM grids or other desired target using the poly (methyl methacrylate) (PMMA) method. The transfer process involved several steps.

First, a PMMA solution was prepared and spin-coated onto the mica substrate at a speed of 3,000 rpm for 60 seconds. The coated mica was then heated at 100°C for 5 minutes.
Next, a second round of PMMA coating was performed on the mica substrate. The PMMA solution was spin-coated at a lower speed of 1,000 rpm for 60 seconds, followed by heating at 100°C for 5 minutes to ensure the adhesion between the sample and increase the thickness of the PMMA film.

To transfer the PMMA film along with the samples from the substrate, blue tapes is stacked along the boundary of substrate for assisting transfer. We then immersed PMMA/Sample/ substrate in water w. The PMMA film, along with the samples, was carefully stripped off from the mica substrate by assisting with these tapes, ensuring that the samples were securely held within the PMMA film for subsequent transfer.

The PMMA film containing the sample is fished out by the desired target. To remove any remaining water and promote adhesion, the grids or substrates with the PMMA film were baked at 60°C for 10 minutes.

Finally, the target was immersed in acetone to dissolve and remove the PMMA film. This step allowed the samples to be readily available for further analysis and characterization.

2.4 Experimental Apparatus and Characterization Techniques

2.4.1 Optical characterization

2D thin films prepared using the CVD method on SiO_2/Si substrates exhibit clear features with different colors compared to the substrate. The color variation can provide approximate information about the thickness and morphologies of the films, where the color gradually changes from thickness increasing due to different reflective index of wavelength. Therefore, the fabrication of In_2Se_3, MoS_2, WS_2, and MoS_2/WS_2 heterostructures, optical microscopy employed to observe the surface morphology of the samples. This includes examining the color intensity, shape, and grain size of 2D materials. Observation of the thin films is crucial as it allows us to understand the growth conditions and optimize the growth process by adjusting experimental growth parameters. The optical microscopy as shown in Figure 2.3.

Figure 2.3 Nikon optical microscope in laboratory of department of applied physics

2.4.2 Raman measurement

Raman spectroscopy is a powerful analytical technique that provides information about the vibrational and rotational modes of molecules in 2D material. Raman signal produced by incident laser beam shown as a fingerprint for identifying the chemical composition of the material. The Raman peaks of 2D MoS_2 and WS_2 thin films primarily originate from two vibration modes: in-plane (E^1_{2g}) and out-of-plane (A_{1g}). The frequency difference between the peaks allows for a rough estimation of the number of layers of the film. The typical default condition of Raman spectroscopy is set as 532 nm wavelength laser, and the 1mW of power.

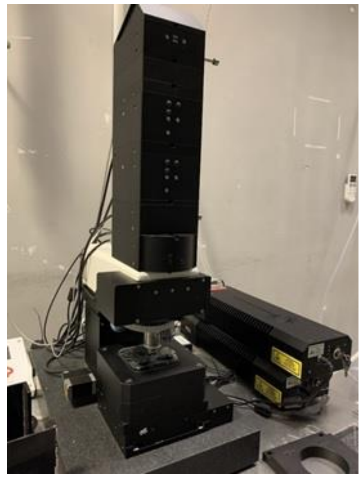

Figure 2.4 WITEC confocal raman in laboratory of the AP department

2.4.3 Transmission electron microscopy

Transmission Electron Microscopy (TEM) is an advanced imaging technique that utilizes a beam of electrons to visualize the internal structure of materials at the nanoscale. The high-energy electron beam is transmitted through a specimen, and the resulting interaction between the electrons and the sample provides detailed information about its composition, crystal structure, defects, and morphology. TEM achieves much higher resolution than conventional light microscopy, enabling the visualization of atomic-level details. It also allows for the acquisition of selected area electron diffraction (SAED) patterns and energy dispersive x-ray spectrometer which offer important information on crystallinity and elemental analysis.

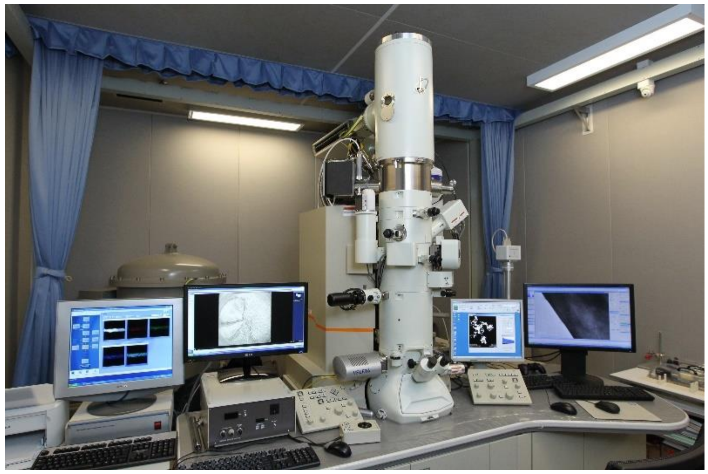

Figure 2.5 JEOL JEM-2100F TEM installed in laboratory of Centre for Electron Microscopy

Chapter 3. Growth and Characterization of In_2Se_3

In this chapter, the CVD method will be employed to fabricate In_2Se_3 thin films on various substrates. Optical microscopy and other characterization techniques will be utilized to analyze and characterize the samples. Furthermore, the growth conditions, such as growth time, precursor quantities, and source-substrate distance, will be optimized to produce high-quality single-crystal β'-In_2Se_3.

3.1 Conventional and Van der Waals epitaxies of on various substrate

The CVD system for the growth of indium (III) selenide was operated at atmospheric pressure, 1 atm. An Ar gas atmosphere was maintained throughout the process to ensure an inert environment and prevent oxidation. The precursor material was high-purity indium (III) selenide (99.99%), sourced from Innochem. A series of experiments were conducted to optimize key parameters, such as the substrate, reaction duration, the quantity of the precursor, and the distance between the source and the substrate. The specific values tested for each experiment, as ranges tested (Table 3.1, Table 3.2, and Table 3.3), are documented in the relative chapter alongside the result.

3.2 Growth condition optimization for single crystal In_2Se_3

In this experiment, CVD synthesis was conducted on various substrates, including silicon dioxide, mica, silicon, highly oriented pyrolytic graphite (HOPG), and sapphire. The synthesis was performed at different temperatures ranging from 780°C to 860°C to investigate the growth behavior of the 2D thin films. Detail experimental conditions can be seen in table 3.

Among the substrates tested, it was observed that the mica substrate yielded the best results in terms of film growth. The samples grown on mica exhibited desirable characteristics such as uniformity, smoothness, and a well-defined crystal structure.

However, it was noticed that all substrates experienced an undesirable phenomenon when subjected to a high temperature of 840°C. At this temperature, black dots appeared on the surface of the samples, indicating an unfavorable condition for the growth of 2D thin films.

The formation of black dots at high temperatures can be attributed to several factors. One possible reason is the presence of impurities or contaminants on the substrates or in the CVD reactor. These impurities may react with the precursor gases at elevated temperatures, leading to the formation of unwanted by-products or nucleation sites.

Another reason could be the occurrence of thermal decomposition. At higher temperatures, the defect density of the material is increased, which can result in defect favorable phase of In_2Se_3, for example, the γ phase is more stable than that of α and β phases in high temperatures(*3*). This instability of the sample may be due to the escape of high-temperature selenium and creates plenty of defects in the material. Therefore, the van der Waals structure collapsed into the bulk island as shown in Figure 3.1.

To solve these issues, further optimization of the CVD growth parameters, such as growth time, mass quantity, and source substrate may be necessary.

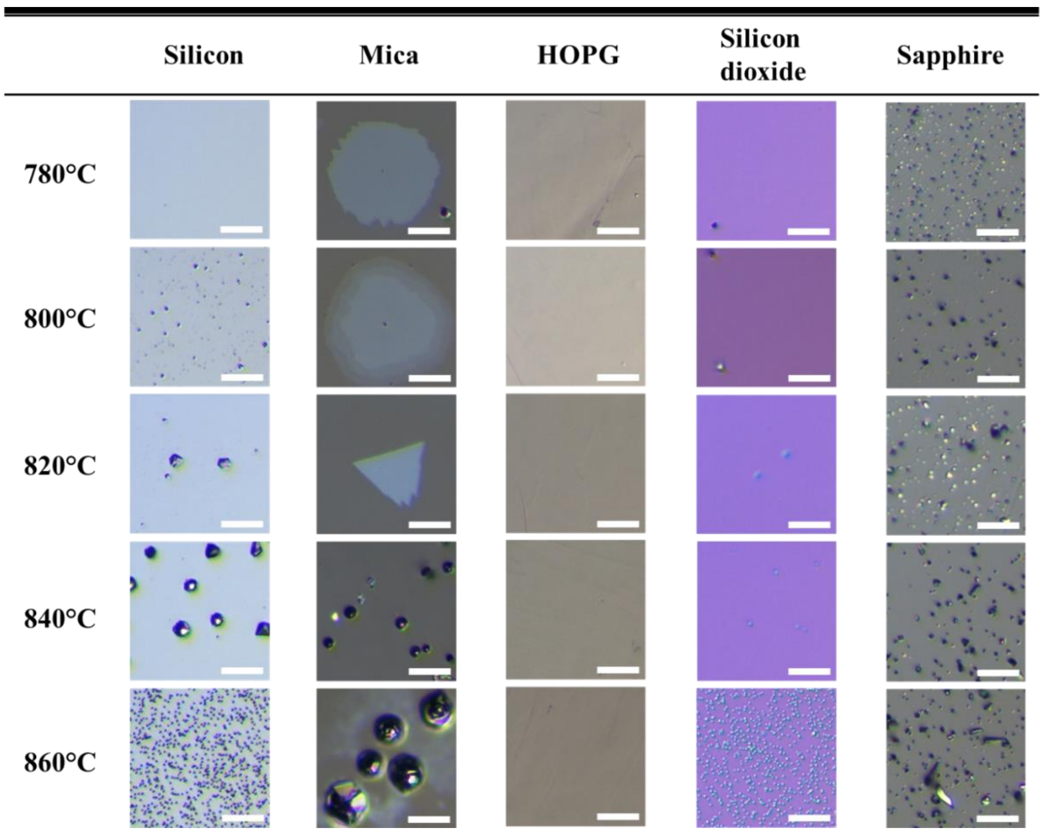

Figure 3.1 Influence of substrate and temperature on CVD Synthesis of 2D thin films. The scale bar is 10 μm.

3.2.1 Optimization of reaction duration

In continuation of the previous study on the influence of substrates and temperature on the CVD synthesis of 2D thin films, the duration of the synthesis process was further investigated. The duration of the synthesis was varied from 0.1 minutes to 40 minutes to explore the effects of growth time on the characteristics of the thin films.

Figure 3.2 are the result of synthesis, it was observed that as the synthesis time increased, the occurrence of black dots reappeared on the surface of the samples. This indicated that an extended growth duration had a detrimental effect on the quality of the 2D thin films. The presence of black dots suggested the formation of defects or impurities in the growing films.

Interestingly, at shorter growth times of around 10 minutes and 15 minutes, the films exhibited larger lateral sizes compared to shorter durations. This indicated that a moderate growth time allowed for the expansion of the thin films in terms of their lateral dimensions.

However, as the growth time was further prolonged to 20 minutes, the films started to become thicker. This increase in thickness may be attributed to the continued deposition of precursor species onto the existing film surface. Consequently, the excessive thickness resulted in a decrease in the lateral size of the films, possibly due to increased surface diffusion and rearrangement of atoms during prolonged growth, or edge decomposition.

Table 3.1 Duration for In_2Se_3 growth

	Temperature for In_2Se_3 (°C)	Gas flow of argon (sccm)	Holding time (min)	Quantity of In_2Se_3 (mg)	Substrate size (mm x mm)
Duration of reaction	800	30	**0.1**	65	10 x 10
			5	64.9	10 x 10
			10	65.1	10 x 10
			15	65.2	10 x 10
			20	65.2	10 x 10
			25	64.9	10 x 10
			30	65.1	10 x 10
			40	65.1	10 x 10

Table 3.1 provides the durations for which the In2Se3 growth reactions were carried out under specific CVD conditions.

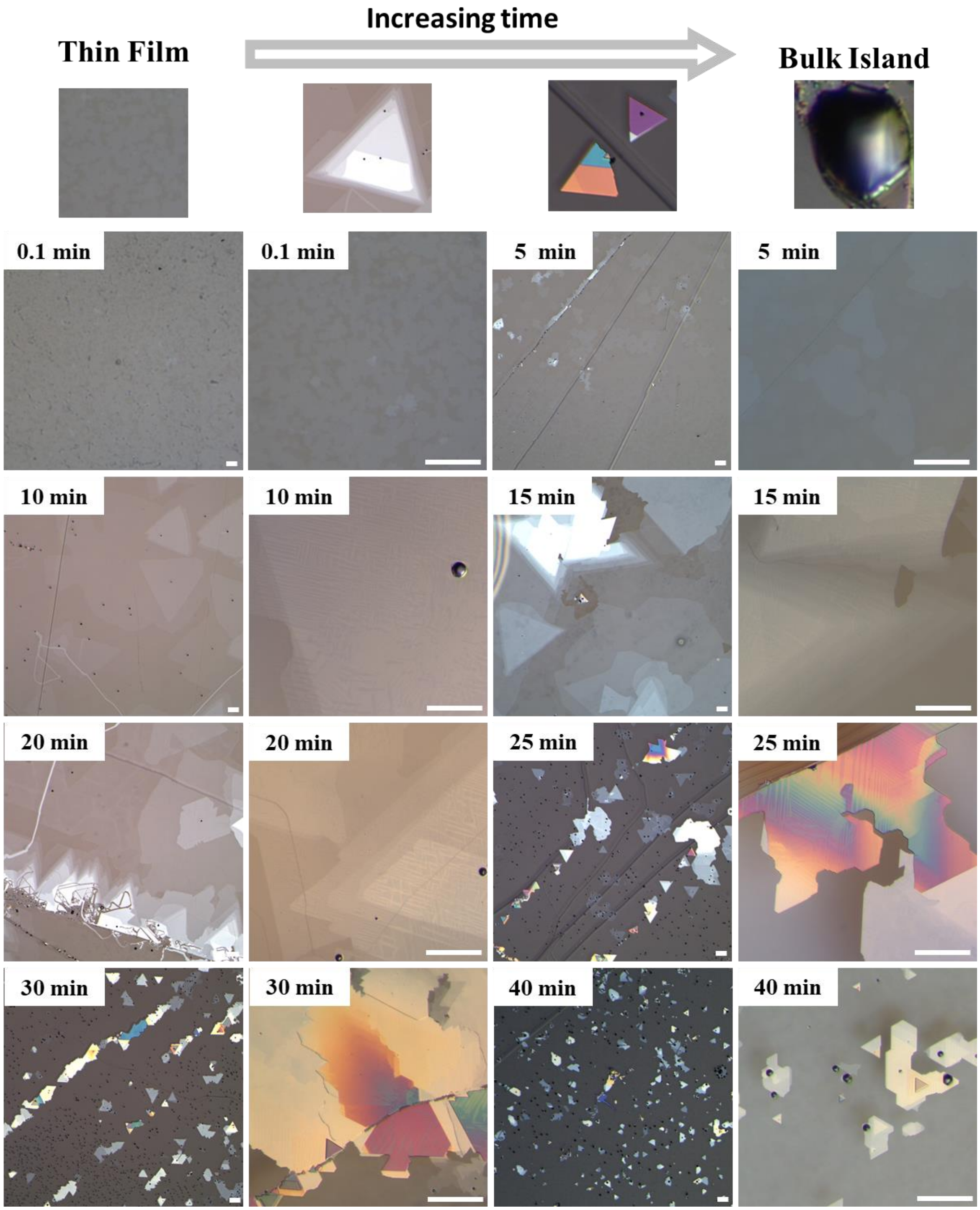

Figure 3.2 Influence of time duration on CVD Synthesis of 2D thin films. The scale bar is 40 µm.

3.2.2 Optimization of precursor quantity

Following the investigation into the influence of substrate, temperature, and time on the CVD synthesis of In_2Se_3, the quantity of source material was examined. Three different amounts of source material, namely 35 mg, 65 mg, and 95 mg, were used to explore their impact on the characteristics of the In_2Se_3 thin films.

It was observed that when using 35 mg of source material, defective films were formed. These films exhibited etching-like features at the edges, and the boundaries did not display the typical triangular or hexagonal shapes associated with 2D materials. This suggests that the lower quantity of source material hindered the growth process, resulting in the formation of flawed films.

In contrast, when using 65 mg and 95 mg of source material, the samples of In_2Se_3 exhibited similar characteristics. However, it was noted that the film synthesized with 95 mg of source material showed a higher density of nucleation sites. This was evident through the observation of a greater number of islands during the growth process.

Table 3.2 Precursors quantity for In_2Se_3 growth

	Temperature for In_2Se_3 (°C)	Gas flow of argon (sccm)	Holding time (min)	Quantity of In_2Se_3 (mg)	Substrate size (mm x mm)
Mass transport	800	30	10	**35**	10 x 10
				65.1	10 x 10
				95.1	10 x 10

Table 3.2 provides the precursor quantity for which the In2Se3 growth reactions were carried out under specific CVD conditions.

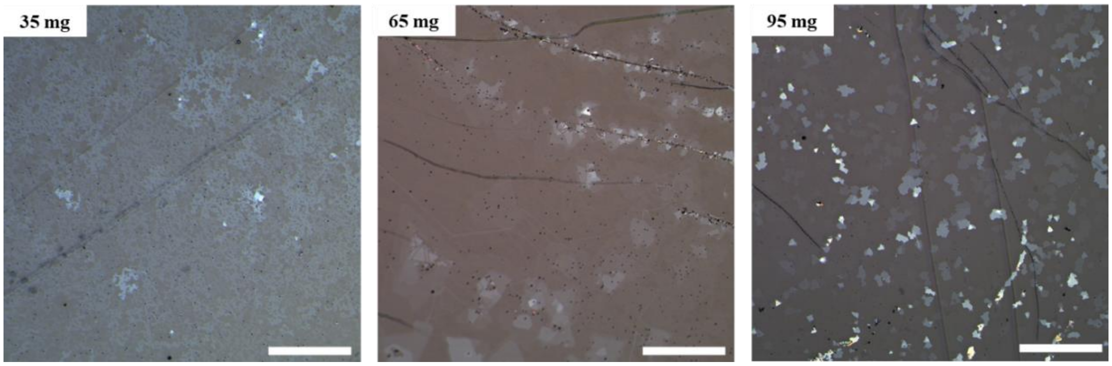

Figure 3.3 Influence of source quantity on CVD synthesis of 2D thin films. The scale bar is 200 µm.

3.2.3 Optimization of source distance

As a final step in the study, the source-to-substrate distance was adjusted by using larger mica substrates compared to smaller ones. Due to the fixed size of the container, a 10mm*10mm substrate was initially used, and the source distance was measured to be 3mm. Subsequently, a larger 25mm*15mm substrate was utilized, resulting in an increased source distance of 5.5mm. In figure 3.4, the grown with the 10mm*10mm substrate at a source distance of 3mm exhibited defective film. These defects were noticeable as the film thickness was significantly thicker compared to the films grown with the larger substrate. Additionally, the film grown with the 10mm*10mm substrate showed a larger lateral size.On the other hand, the films grown with the 25mm*15mm substrate at a source distance of 5.5mm displayed a higher density of nucleation sites. However, these films appeared smaller and thinner compared to the films grown with the smaller substrate.

Table 3.3 source-substrate distance for In_2Se_3 growth

	Temperature for In_2Se_3 (°C)	Gas flow of argon (sccm)	Holding time (min)	Quantity of In_2Se_3 (mg)	Substrate size (mm x mm)	source-substrate distance(mm)
Source distance	800	800	10	95	**10 x 10**	**3 mm**
					25 x 15	**5.5 mm**

Table 3.2 provides the source distance for which the In2Se3 growth reactions were carried out under specific CVD conditions.

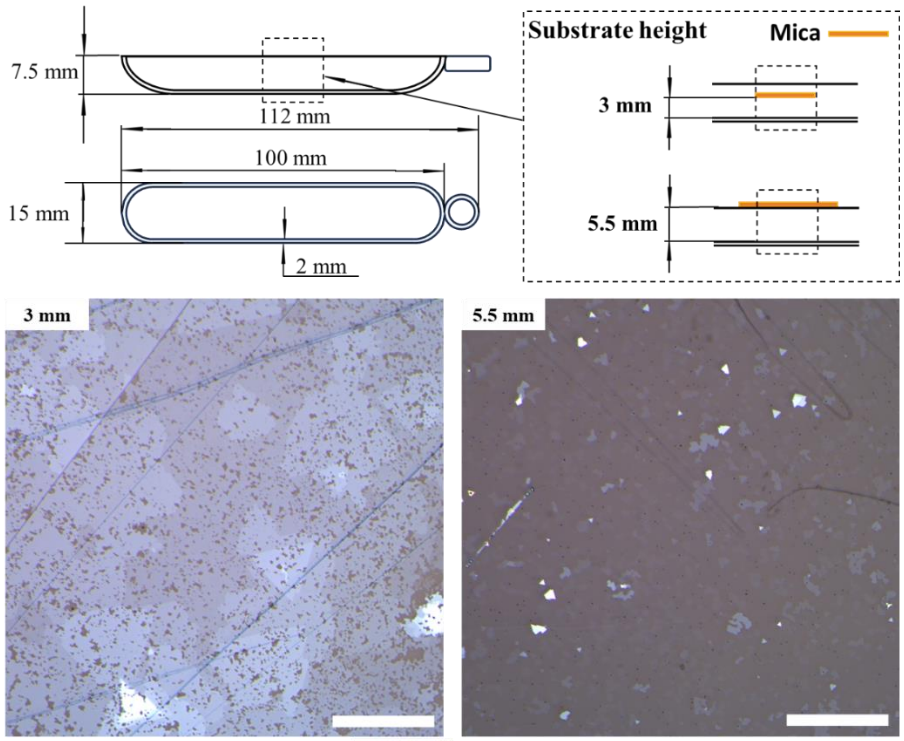

Figure 3.4 Schematic design of source-to-substrate height by substrate size control. The scale bar is 200 µm.

3.3 Phase transition between α-In_2Se_3 and β'-In_2Se_3

An interesting observation was made regarding the behavior of the samples after the cooling process. It was noted that some of the samples formed an ordered network structure, which exhibited curling or buckling at the boundaries in figure 3.5. These distinct features were clearly visible in the optical images of the samples. The formation of curling or buckling boundaries suggests the presence of mechanical stresses within the thin films. During the cooling process, as the difference of thermal expansion coefficient between the films and substrate, films contract or tensile, and the mechanical forces within the film can lead to deformations which overcome the energy barrier and trigger the phase transition mechanism between α-In_2Se_3 and β'-In_2Se_3.

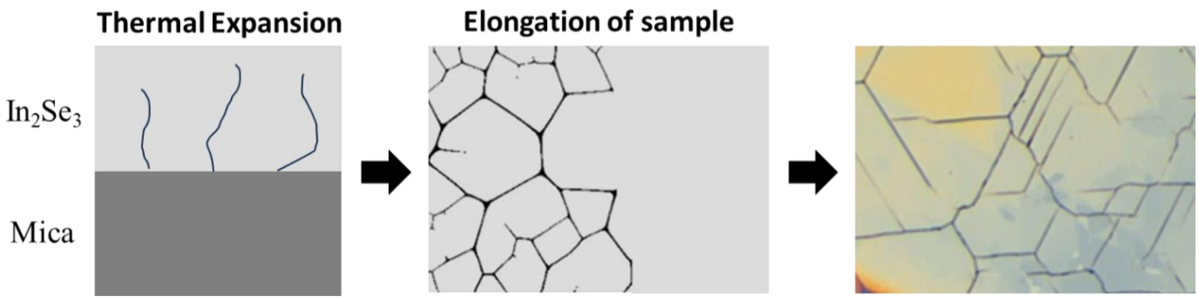

Figure 3.5 Schematic of cooling effect inducting of phase transition between α-In_2Se_3 and β'-In_2Se_3.

Further analysis using Raman spectroscopy in figure 3.6 provided valuable insights into the structural characteristics of the observed buckling network and the surrounding uniform area. The Raman spectra revealed distinct differences in the peaks corresponding to the alpha and beta phases of the thin film material. In the buckling network region, the Raman spectra exhibited characteristic peaks corresponding to the α-In_2Se_3, 104 cm^{-1} A_1^1 vibrational mode. This indicates that the buckled regions have a different structural arrangement compared to the surrounding uniform area, which is predominantly in the β' and β -In_2Se_3, having Raman peak near 110 cm^{-1} A_{1g}^1.

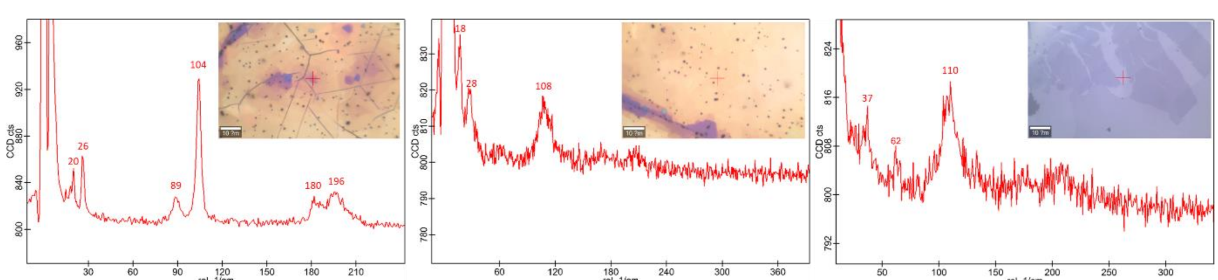

Figure 3.6 Raman spectroscopy analysis of the buckling and uniform regions in the thin film

Selective area diffraction patterns were obtained from the thin film samples after the PMMA transfer process. Notably, significant differences were observed between the diffraction patterns of the uniform film and the buckling network area.

In the diffraction pattern of the uniform film, super spots corresponding to the secondary structure of the material were clearly visible. These superspots are marked by dot line blue rectangular. It is typically considered as a signature of the β'-In_2Se_3. This finding suggests that the uniform film predominantly consists of the beta phase, which is known for its distinct structural arrangement and properties. On the other hand, the diffraction pattern of the buckling network area exhibited a perfectly symmetric pattern of α-In_2Se_3 they provide there are differences in phase.

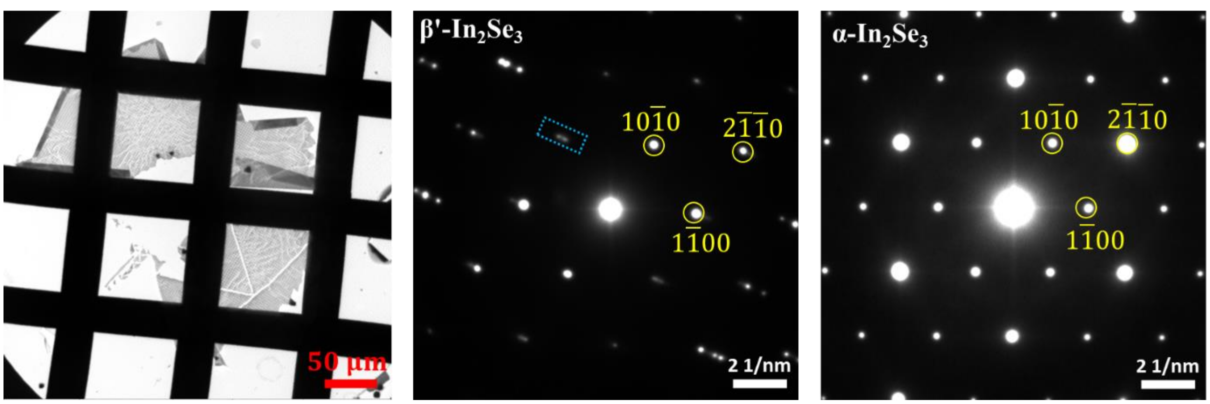

Figure 3.7 Low magnification of TEM, and selective diffraction pattern for buckling and uniform region

3.3.1 domain wall of β'-In_2Se_3

Polarized optical microscopy was employed to observe the In_2Se_3 thin film and reveal the presence of in-plane polar domains within its structure. Notably, the behavior of domain walls in relation to cracking regions was investigated. Upon observation, it was found that the domain walls appeared dense in density when they were located further away from the cracking regions. This suggests a strong correlation between the domain wall distribution and the film's structural integrity. The dense presence of domain walls in these areas indicates a well-ordered and stable structural arrangement. However, an interesting phenomenon occurred when the domain walls were located near the cracking region. In these regions, the domain walls seemed to disappear. This disappearance of the domain walls near the cracking region is believed to be associated with a phase change in the thin film.

Specifically, it is hypothesized that the domain walls near the cracking region transform into an out-of-plane alpha phase. This phase change could be induced by the local stress concentration caused by the cracking. The presence of cracks in the thin film may disrupt the structural alignment and lead to a transformation of the in-plane polar domains into the out-of-plane alpha phase.

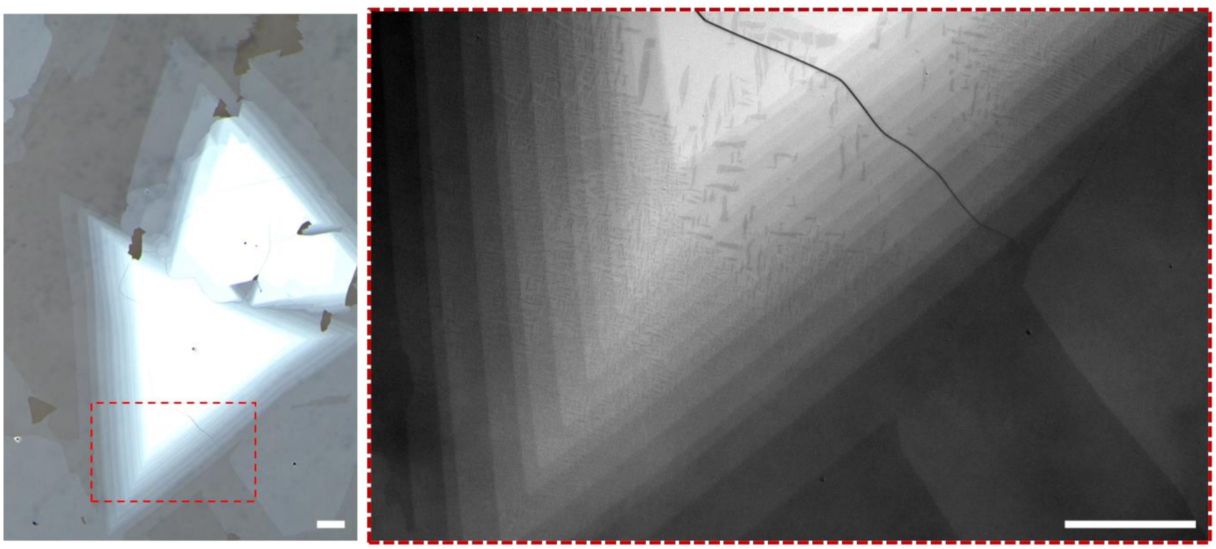

Figure 3.8 Polarized optical microscopy of as growth sample with cracking inducing phase transition. The scale bar is 40 μm.

3.3.2 Dynamic Phase transition phenomena

We recorded a video to capture the dynamic phase transitions within the In_2Se_3 thin film. These recordings provided valuable insights into the phase changes occurring in real-time, as evidenced by contrast variations and the appearance of a blocking network structure. The formation of this blocking network structure is believed to indicate the development of a heterostructure within the film by thermal expansion.

In another video recording, external forces were applied to the material to induce mechanical stress and observe the resulting phase transitions, while bending the thin film showing the left of sample from the substrate, that the phase transition can be freely deformed without forming buckling network. In visualization of the dynamic phase transitions under a microscope. The results of these experiments revealed fascinating observations. As the external forces were applied, the previously stable phase of the thin film underwent a dynamic transition. This transition was characterized by changes in contrast and the emergence of the blocking network structure. The appearance of contract difference indicated the formation of a heterostructure, likely due to the rearrangement of atoms and changes in the crystal structure, but we can hardly to chase the propagation of phase transition in TEM, the optical record of the propagation speed of atomic chain reaction may be meaningful to application.

The in-plane strain retained within as-grown samples is predominantly a result of cooling-induced strain coupled with the disparity in thermal expansion coefficients between the 2D film and the substrate material. Specifically, the expansion coefficients for α-In_2Se_3 is approximately $10\times10^{-6}K^{-1}$, and the material exhibits a lattice constant of 4.16 Å. (*51*)
In contrast, fluorophlogopite mica, a substrate commonly employed for the growth of such films, has a expansion coefficients of about $6.3\times10^{-6}K^{-1}$ at 600°C, and features a surface hexagonal lattice constant of 5.308 Å for the (Si^{4+}/Al^{3+}) tetrahedral layers, (*52, 53*)which is substantially larger than that of In_2Se_3. Despite the significant differences in their lattice dimensions, this disparity does not result in pronounced strain or the emergence of defects.

The greater expansion coefficient of α-In_2Se_3 relative to that of fluorophlogopite mica induces a tensile strain within the film during cooling from high-temperature synthesis. The surface adhesion mediated by vdW forces contributes to the stabilization of the β'-In_2Se_3 phase post-cooling. This tensile strain, however, may be alleviated when the 2D films undergo transfer onto non-flat or uneven substrates or experience local detachment events such as those observed during ex-situ bending, as illustrated in the associated Figures 3.9.

Determining the exact strain energy involved in these processes is challenging. Research into analogous systems, such as the contact-splitting transfer of graphite from hexagonal boron nitride BN to MoS_2, has revealed an energy barrier for detachment as high as 26 meV/Å^2(*54*). Given the similarity in vdW layered interfaces, the strain energy at the interface between mica and α-In_2Se_3 may be comparable, suggesting a potential similarity in the energy barriers involved in these material systems. Thus, the strain energy may be on the around a few tens of meV/Å^2 which is less than the energy barriers.

Despite the efforts made, the complete and reversible phase transition in 2D In_2Se_3 remains largely unclear. To address this, we employed Density Functional Theory (DFT) calculations to examine the phase stability as a function of layer number and strain (Figure 3.10). The results indicate that the α and the β' phase have close energies. The energy of the α phase is slightly lower than that of the β' phase. DFT calculations predict that the β' phase will dominate over the α phase under tensile strain, regardless of thickness, a finding that is consistent with experimental observations.(*18*)

Our study of the dynamic phase transitions in In_2Se_3 reveals that the antiferroelectric β' phase and the ferroelectric out-of-plane α phase coexist in 2D In_2Se_3. This coexistence is not due to interlayer mixed stacking, as seen in other research, but rather is attributed to the formation of unusual ferroelectric and antiferroelectric interfaces. The research into these unique interfacial properties is scarce, which makes the study of phase transitions between the ferroelectric α phase and the antiferroelectric β' phase, their reversible phase transition, or the coexistence effect at the interface particularly worthy of further investigation.

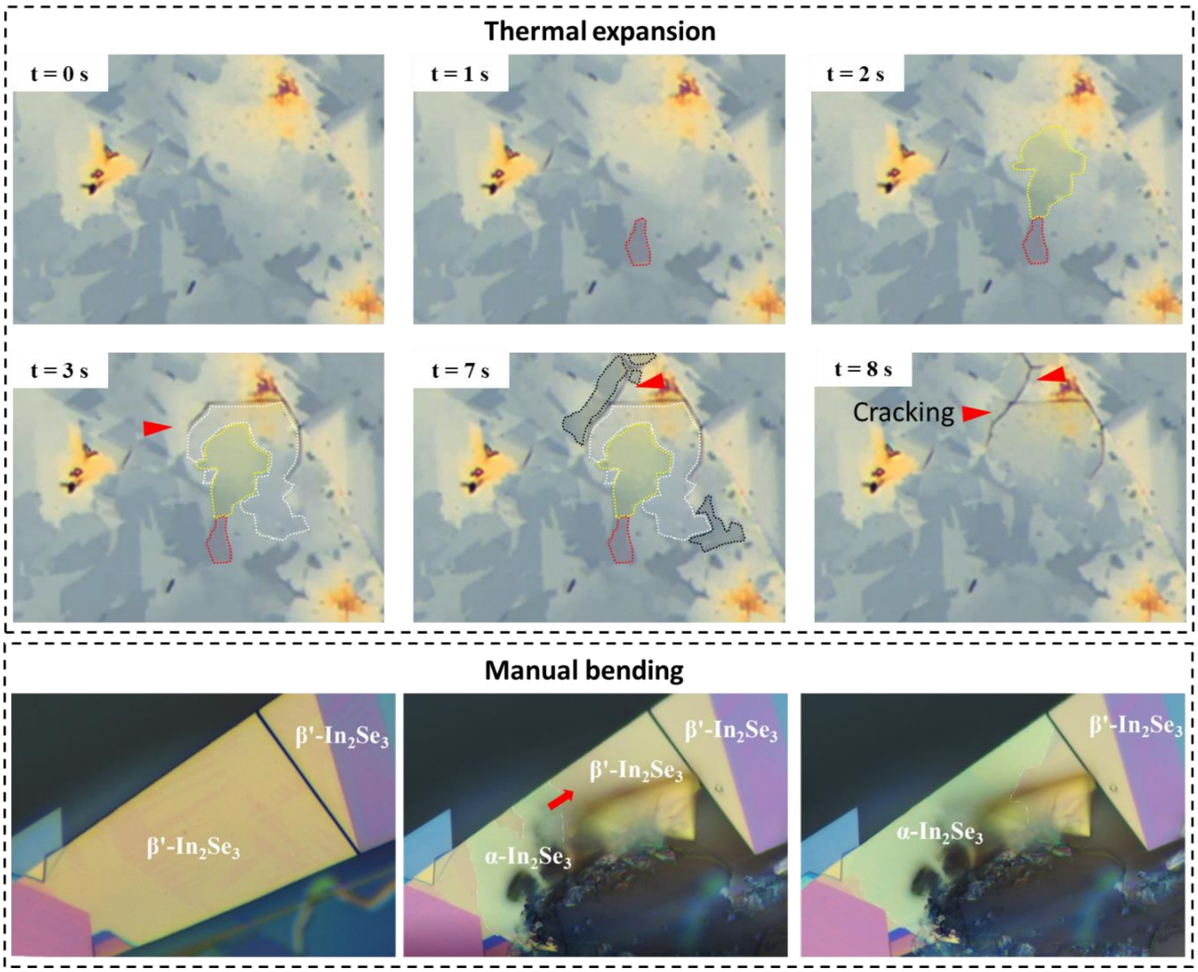

Figure 3.9 Dynamic phase transition phenomena induced by thermal expansion and manual bending.

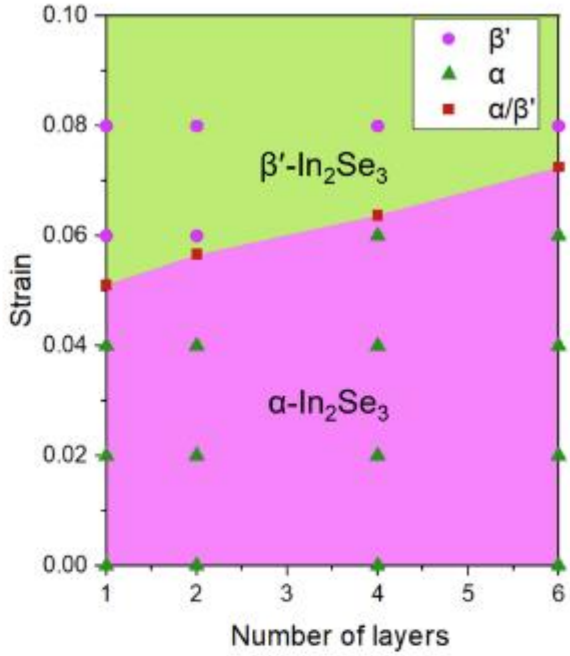

Figure 3.10 Phase diagram of α-In_2Se_3 and β′- In_2Se_3 on strain and layer number, obtained by DFT calculations. Image from (*18*)

3.3.3 α-In_2Se_3 - β'-In_2Se_3 heterostructure

Figure 3.10 Raman mapping was performed to further investigate the distribution of interphases within the In_2Se_3 thin film. By providing a comprehensive view of the spatial distribution of interphases, the Raman mapping results provided further validation for the previous findings.

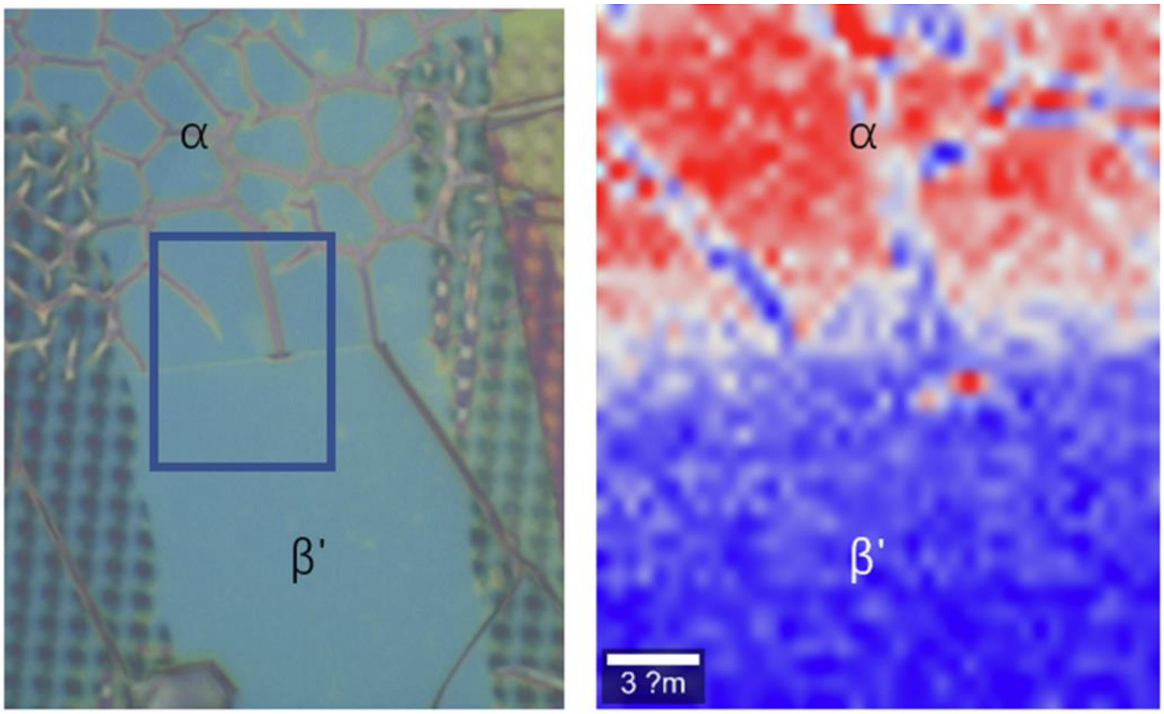

Figure 3.11 Raman mapping of the heterostructure

Chapter 4. Fabrication of MoS_2-WS_2 heterostructure

4.1 Reproducible control of MoS_2 and WS_2 CVD growth utilizing metal oxide powder

The interphase of In_2Se_3 is uncertain due to its transition mechanism. If we investigate the atomic structure of the interphase, investigating the MoS_2-WS_2 boundary may be appropriate since its interior structure is separated due to sequential growth CVD, and the junction can be clearly resolved.In this session, CVD methods will be employed to synthesize MoS_2 and WS_2 separately. The growth conditions will be further optimized for the sequential growth of a heterostructure involving both materials. The ultimate goal is to investigate the interphase structure between the two materials.

Initially, the growth of MoS_2 will be synthesized using conventional CVD without the aid of salt. However, it has been observed that the deposition rate and growth behavior on the silicon wafer are affected by the temperature and the amount of MoS_2 source used.

4.1.1 From polycrystal to single crystal of MoS_2

We employed CVD methods to synthesize high-quality monolayer MoS_2. The synthesis involved vaporizing solid powder forms of molybdenum trioxide and sulfur in an argon atmosphere (*55*). The deposition process facilitated the growth of a thin MoS_2 layer on a SiO_2/Si substrate through the occurrence of the following equation(*55*):

$$2MoO_3 + 7S \rightarrow 2MoS_2 + 3SO_2$$

Recent research has made significant improvements in understanding the overall reactions involved in the synthesis of MoS_2, revealing two essential intermediate steps: chemical reduction and continuous sulfurization. The process occurs under high thermal conditions within a furnace, where the powdered form of MoO_3 undergoes melting and subsequent evaporation as a reactive gas, transitioning into a vapor state. As the temperature increases, the concentration of $MoO_{(3-x)}$ vapor within the reaction chamber also rises. Nucleation sites are formed on the surface of SiO_2/Si, which acts as a stable adsorption site for the reactants. Subsequently, under a rich supply of sulfur, the $MoO_{(3-x)}$ species is further sulfurized, leading to the formation of nanoflakes of MoS_2. The elemental steps involved in this process are outlined below(*56, 57*):

$$\text{Reduction:} \qquad 2MoO_3 + xS \rightarrow MoO_{(3-x)} + xSO_2$$

$$\text{Sulfurization:} \qquad MoO_{(3-x)} + (7-x)\,S \rightarrow 2MoS_2 + (3-x)SO_2$$

To achieve high-quality thin films of MoS_2, researchers have been continuously improving the CVD method. One common approach is the molten salt-assisted CVD(*58*), which has been widely used for the growth of various TMDs, including MoS_2 and WS_2.This method involves the use of a salt that alters the reaction pathway, leading to the formation of intermediate reactants with lower melting points. This modification facilitates the synthesis of large-area, high-quality thin films at an increased growth rate. In subsequent sessions, this method will also be employed for the synthesis of WS_2 and its heterostructures.

The CVD setup for MoS_2 synthesis in this study involved two heating zones, different from the physical vapor deposition of In_2Se_3. Each is responsible for heating sulfur and MoO_3 separately. This arrangement indirectly controlled the concentrations of the respective precursors. The gas system utilized only argon gas for MoS_2 synthesis. The reaction took place within a quartz tube, as illustrated in Figure 2.1. During the experiments, a quartz boat containing 4-2 mg of MoO_3 powder was placed in the middle of zone 2, which was located 20 cm away from the container holding 100 mg of sulfur powder upstream in the zone 1. The SiO_2/Si substrate, with a polished 285 mm thickness of SiO_2 layer, was positioned facing downward towards the MoO_3 powder, leaving a 3 mm height gap.

The gas system configuration is shown in Figure 2.1. Before conducting the experiments, it was ensured that the valves were tightly sealed, and the tube was purged with 300 sccm of high-purity Ar gas for 10 min. This step was performed to remove any residual air within the tube. The temperature profiles for the two heating zones were set according to the values outlined in Table 4.1. The heating-up time and holding time followed the temperature schematic plotted in Figure 2.2, specifically stages (i) and (ii) respectively. Zone 2 reached a temperature range of 680-660°C with a rapid ramping rate of up to 41°C per minute. The intermediate species of MoO3-x evaporated quickly and deposited onto the substrate, where sulfurization took place. Sulfur vapor was carried by flowing argon gas.

The entire system operated at atmospheric pressure while maintaining high temperatures. The Mo and S precursors were favourable to the formation of MoS_2 under these conditions. Three primary growth modes: layer-by-layer, Stranski-Krastanov, and island growth modes. The predominant growth mode was primarily determined by the local Mo concentration, while the S concentration remained relatively stable due to comparable transport distances in the upstream. The distance between the substrate and precursor directly determines the concentration of reactive gaseous. This relationship can be simplified using the following equation:

$$C_g(d,t) = C_g(0,t) \times e^{-\left(\frac{d^2}{4Dt}\right)}$$

Given that C_g is the concentration at specific distance and time, D is the diffusion constant. the distance between the substrate and precursor increases, the concentration of gaseous decreases exponentially that cause various morphology of sample produced as variation of Mo precursor concentration. The growth modes are deduced based on rapid change in concentration as the result shown in Figure 4.1, alongside corresponding optical microscopy images displaying a set of large fields of view and higher magnification.

We conducted experiments to investigate the impact of temperature and the quantity of Mo precursor on the preparation of MoS_2 thin films. By slightly reducing the amount of Mo2 precursor, we observed notable changes in the overall morphology and growth. In regions where the deposition of MoS_2 was oversaturated(*59, 60*), the substrate exhibited a circular distribution pattern, resembling island growth, as evident from the black circular features observed in the large-view optical microscopy (OM) images. Interestingly, when using half the quantity of Mo precursor, there was a significant reduction in the growth of specimens in the center of the MoS2 film, while the edge of the substrate displayed similar growth features under the same temperature conditions (680°C), resulting in the formation of a single crystal area of up to 200 µm in Experiment 1 and Experiment 2, as observed in the enlarged OM images.

Subsequently, we decreased the growth temperature to 660°C in experiment 3, which showed a more uniform contrast in the large-view OM images compared to experiments 1 and 2. This indicated a more balanced distribution of the metal reactant throughout the substrate, avoiding an oversupply in the central region. We conclude that the lateral size of monolayer MoS_2 single crystals increases with higher temperatures in Experiments 1 and 2, reaching up to 200 µm, significantly larger than 20 µm in Experiment 3, as demonstrated in Figure 4.1.

The evaporation of Mo and S sources controls the concentration of reactants and affects the composition ratio of gases in the chamber. Reaction temperature affects the adsorption and desorption processes of reactive gases on the substrate surface influencing the growth rate of MoS_2(*60, 61*).

When the reaction temperature is low (660°C of experiment 3), the evaporation of the precursor is minimal, resulting in lower concentration of $MoO_{(3-x)}$ vapor. As a result, the growth occurs at a slower rate, leading to less nanoflake MoS_2 formation. The growth rate on the substrate surface limit by the Mo supply. Consequently, the lateral size of the triangular MoS2 thin film generated is smaller in experiment 3.

As the reaction temperature increases (680°C, experiments 1 and 2), the evaporating rate of $MoO_{(3-x)}$ is enhanced, leading to higher concentrations and faster reaction rates. This results in an increased number and density of microcrystalline nuclei formed on the SiO_2/Si substrate surface. During the subsequent growth process of MoS_2 nuclei, these nuclei merge with each other, and smaller nuclei gradually disappear due to aggregation. As a result, the lateral size of the obtained MoS_2 thin film gradually increases with the temperature rise.

The lateral growth (increased lateral size) and vertical growth (increased thickness) of MoS_2 on the substrate also involve a competitive relationship. The diffusion of reactants adsorbed on the substrate surface needs to overcome the diffusion barrier on the substrate surface to grow on the substrate surface. On the other hand, it needs to overcome the interlayer barrier to grow on the MoS_2 surface. The substrate temperature greatly influences the adsorption of reactants on the substrate. The adsorption of reactants on the substrate depends mainly on the reaction rate of forming the nanocluster and nucleation. The faster reaction rates lead to the consumption of local substances and cause faster adsorption for refilling. At higher reaction temperatures(680°C), the growth of MoS_2 on the substrate is primarily controlled by interfacial diffusion behaviour. Meanwhile, enhanced desorption rate on the substrate surface at higher temperature. When MoS_2 diffuses on the substrate, it is likely to desorb when migrating to weakly binding sites. In contrast, the defective site induces nucleation because of MoS2 nanocluster strongly bonded. The probability of desorption is therefore lower. When the substrate temperature is high, the desorption of MoS-related atomic groups or molecules from the substrate surface is significantly enhanced. While partially desorbed species collide and rebound back to the substrate surface if high concentration. They tend to re-adsorb at sites with strong nucleation points, overcoming the interlayer barrier and promoting the vertical layer-by-layer growth mode of MoS_2 on the substrate surface(*9, 62*).

Table 4.1 Experimental Condition and Optimization for MoS_2 growth

No. experiment	Quantity of MoO_3 (mg)	Quantity of S (mg)	Temperature for MoO_3 (°C)	Temperature for S (°C)	Holding time (min)	Heating up time (min)	Gas flow of argon (sccm)
1	4	99.9	680	120	10	16	150
2	2	100	680	120	10	16	150
3	2	100	660	120	10	16	150

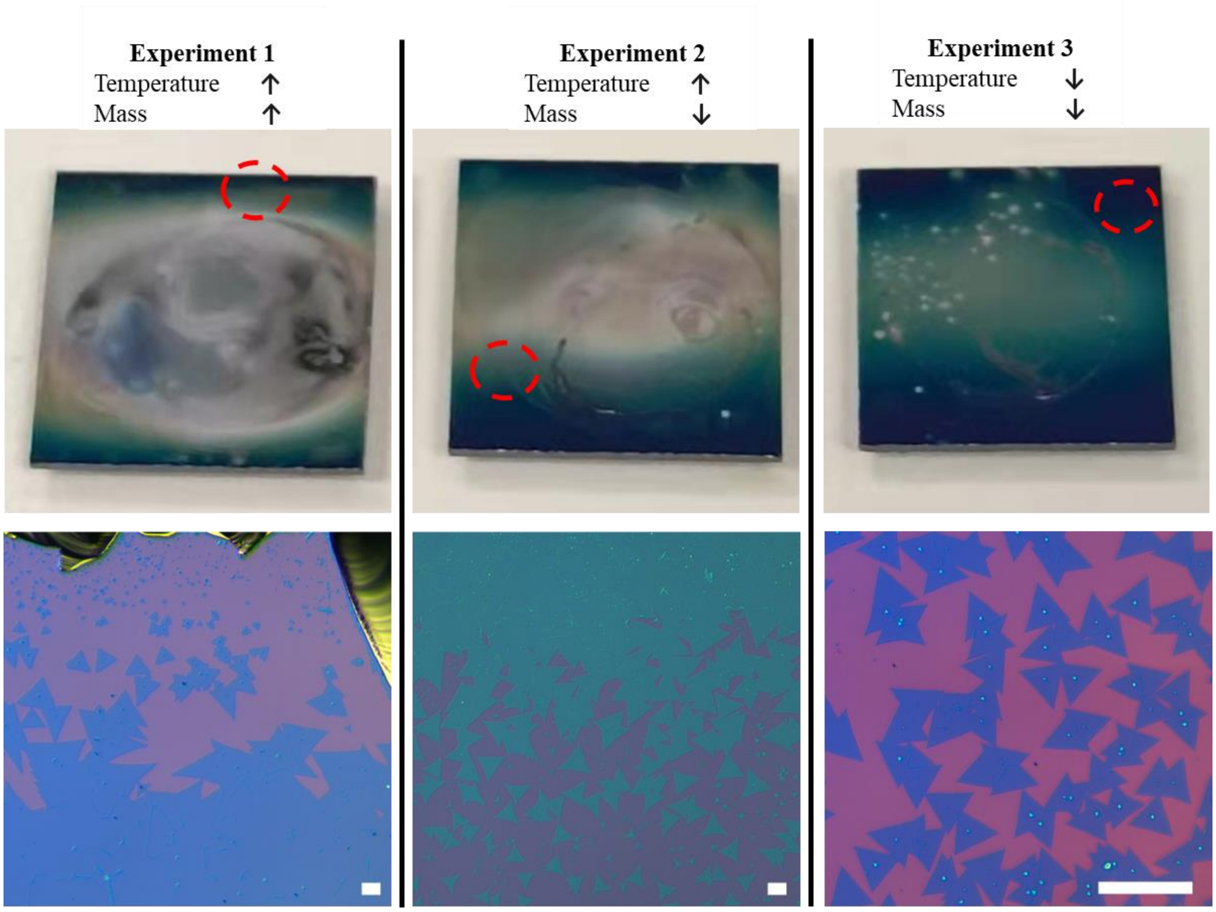

Figure 4.1 The overall view to the 10 mm x 10 mm polished SiO_2/Si substrate and corresponding interest area of expected sample labelled with red circle at large view OM image. The scale bar is 40 µm.

4.1.2 Sodium chloride-assisted catalytic growth of WS_2

The growth temperature plays a crucial role in the growth of WS_2. When a low temperature is used, it becomes challenging to obtain any WS_2 flakes on the substrate, or the synthesized flakes may exhibit poor quality. This is primarily attributed to the high melting points and low vapor pressure of WO_3.

At higher temperatures, it is possible to obtain WS_2 samples with larger sizes, although the flakes may become less stable and prone to thermal decomposition. To address this issue, the use of NaCl has proven effective in reducing the evaporation temperature of the metal oxide

WO_3. During the growth of WS_2, NaCl can react with metal oxide to facilitate the reaction by forming volatile tungsten oxyhalides (Wo_xCl_y) which vaporize at relatively low temperatures(*58, 63-66*) These intermediates can be transported to the substrate surface and subsequently contribute to the growth of WS_2 on the substrate.Moreover, the introduction of a small amount of hydrogen gas has been discovered to significantly improve the quality and morphology of as-grown WS_2 (*56*). Additionally, some researchers have reported that the introduction of NaCl can serve as a growth promoter for the formation of in-plane heterostructures(*67-69*), However, it is crucial to carefully control the timing of NaCl introduction, which will be discussed in the subsequent chapter.

In the experiments, the use of NaCl and hydrogen was found to be essential for the growth of WS_2. SiO2/Si substrate measuring 10 mm x 10 mm was prepared following the **Step 1** substrate preparation method described previously. An ethanol solution containing 0.26 mM of NaCl was uniformly deposited on the SiO2/Si surface and heated in an oven to ensure complete drying. The substrate was then placed on a quartz boat containing 6 mg of WO_3 powder, while a separate quartz boat containing 100 mg of S was positioned 20 cm away from WO_3 in the upstream. After purging with argon gas, a mixture of hydrogen and nitrogen gases was set at a flow rate of 50 sccm. The furnace was operated according to the temperature conditions outlined in Table 4.2, with Zone 1 set at 180°C for S evaporation and Zone 2 at 900°C. Additionally, an annealing stage for 10 min was included in order to enhance the quality of the heterostructure, considering the subsequent sequential CVD process.

The experiments were conducted under identical growth conditions. Without the presence of NaCl, no WS_2 flakes were formed on the substrate. However, when NaCl was added, a significant difference was observed, with the synthesis of large triangular WS_2 flakes. NaCl serves as an important growth factor by increasing the mass flux of the tungsten source. In the growth process of CVD methods, there is a competition between the mass flux of precursors and the reaction rate of lateral and vertical growth. The mass flux controls the nucleation density and growth rate. When the growth rate exceeds the mass flux, larger crystal grain sizes are obtained. On the other hand, when the mass flux is higher than the growth rate, a polycrystalline film is formed (*58, 70*). In Experiment 1, no sample formation was observed due to the limitation of the growth rate and mass supply. However, in Experiment 2, the presence of molten salts, which can form oxychlorides through a reaction, significantly increased the reaction rate. It is believed that the reaction between WO_3 and NaCl in the chamber led to the formation of intermediate compounds such as WO_2Cl_2 (melting point = 265°C) and $WoCl_4$ (melting point = 211°C), The possible catalytic pathway is as follows (*64*).

$$WO_3\,(s)+NaCl(s) \rightarrow NaWO_3(s)+WOCl_4(g)+WO_2Cl_2(g)+WO_2(s)+W(s)$$

$$WOCl_4(g)+WO_2Cl_2(g)+S(g)+H_2(g) \rightarrow WS_2(s)+HCl(g)+H_2O(g)$$

The presence of NaCl aids in the transportation of tungsten to the growth substrates and enhances the mass flux. This, in turn, enables the growth of high-quality WS_2 crystals at a temperature of 900°C.The size of monolayer WS_2 is influenced by the selection of alkali metal halides and temperature. However, our primary objective is to grow a heterostructure, and further optimization falls outside the scope of this session.

Table 4.2 Experimental Condition for WS_2 growth

No. experiment	Addition of NaCl	Quantity of WO_3 (mg)	Quantity of S (mg)	Temperature for WO_3 (°C)	Temperature for S (°C)	Holding time (min)	Gas flow of 95%N_2+5%H_2 (sccm)
1	NO	6	99.9	900	180	5	50
2	YES	6	100	900	180	5	50

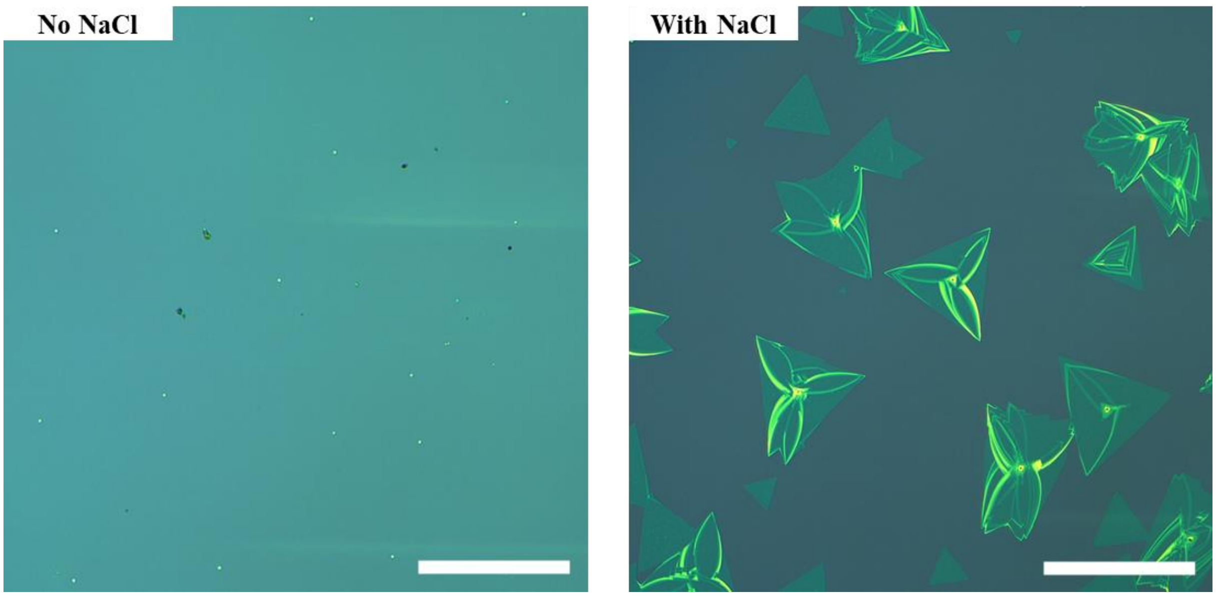

Figure 4.2 The OM morphology of the WS_2 on SiO_2/Si substrate with and without assisting of NaCl. The scale bar is 200 μm.

4.2 Sequential secondary deposition for MoS_2-WS_2 heterostructure

MoS_2 and WS_2 in the previous session, as shown in Tables 4.1 and 4.2, are now being utilized for the sequential CVD method. In the next step, we modify the gas environment by introducing hydrogen at specific time intervals to synthesize the heterostructure, consisting of a MoS2 core followed by the outer layer of WS_2. The implementation of the sequential CVD technique enables precise control over the growth of each composite. However, it is important to note that the ambient conditions may introduce additional uncontrollable factors that could potentially affect the synthesis process.

4.2.1 Influence of gas atmosphere on the Growth on heterostructures

The gas conditions play a significant role in influencing the growth of WS_2 (*56*), Controlling the presence of different gas species allows for the adjustment of the initiation time of the reaction occurrence and ensures appropriate growth within the desired time period while maintaining an effective amount of precursor. Argon and nitrogen gas serves as a protective and carrier gas, facilitating the transportation of the necessary sulfur precursor from the upstream source to the substrate. This ensures that the reaction takes place with sufficient reactant availability. The use of hydrogen as a reducing gas is more effective than sulfur in promoting the reduction of WO_3. It can directly facilitate the reduction process or form H_2S, creating a $WO_{(3-x)}$ rich environment that is promote to the growth of WS_2.

The gas conditions were controlled according to the provided Table 4.3. As an example, experiment 2 involved running the process with 250 sccm of Ar for the first 40 minutes, and then switching to 50 sccm of H_2+N_2 at the 40 min mark, as depicted in the schematic diagram in Figure 4.3.

In Figure 4.4, the substrate (55min Ar: 10 min H_2+N_2) is observed to be filled with irregular dot specimens, indicating high nucleation sites due to oversaturated W precursor concentration. This leads to the formation of intermediate impurity sites on the surface. Moreover, when only argon gas (65min Ar: 0 min H_2+N_2) is used for the synthesis of the WoS_2-MoS_2 heterostructure, it forms a thickness boundary of WS_2 at the edges and residual impurity dots on the substrate. Possible island growth mode is favourable at these conditions.

By selecting a gas supply time of (50 min Ar: 15 min H_2+N_2), and (45min Ar: 20 min H_2+N_2), The nucleation density decreases while tending to form the desired lateral heterostructure. Further optimization is achieved using a gas supply recipe of (45 min Ar: 25 min

H_2+N_2), which yields repeatable results as shown in Figure 4.4 and Figure 4.5. This suggests that the appropriate gas supply can facilitate the re-activation of the inert boundaries cause by the exposed ambient environment. It likely forms the monolayer lateral heterostructure.

When using pure H_2 and N_2 (0 min Ar: 65 min H_2+N_2), a low yield of heterostructure is observed. Additionally, instead of sequential lateral growth, the WS_2 tends to aggregate as dots at the boundaries. This phenomenon could be attributed to the depletion of reactants over a prolonged reaction time with H2 gas, which limits the mass transport to the substrate.

Table 4.3 Control of gas atmosphere

No. of experiment	Gas conditions: Argon supply (250 sccm) / 5%H_2 + 95%N_2 supply (50 sccm)
1	Start with H_2 + N_2
2	Switch from Argon to H_2 + N_2 at 40 min
3	Switch from Argon to H_2 + N_2 at 45 min
4	Switch from Argon to H_2 + N_2 at 50 min
5	Switch from Argon to H_2 + N_2 at 55 min
6	Do not switch to H_2 + N_2

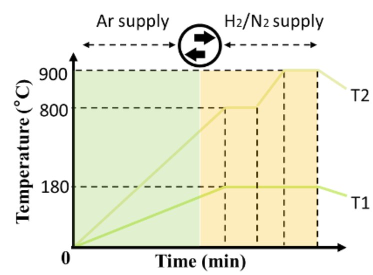

Figure 4.3 Schematic of Timeslot for switching the gas conditions

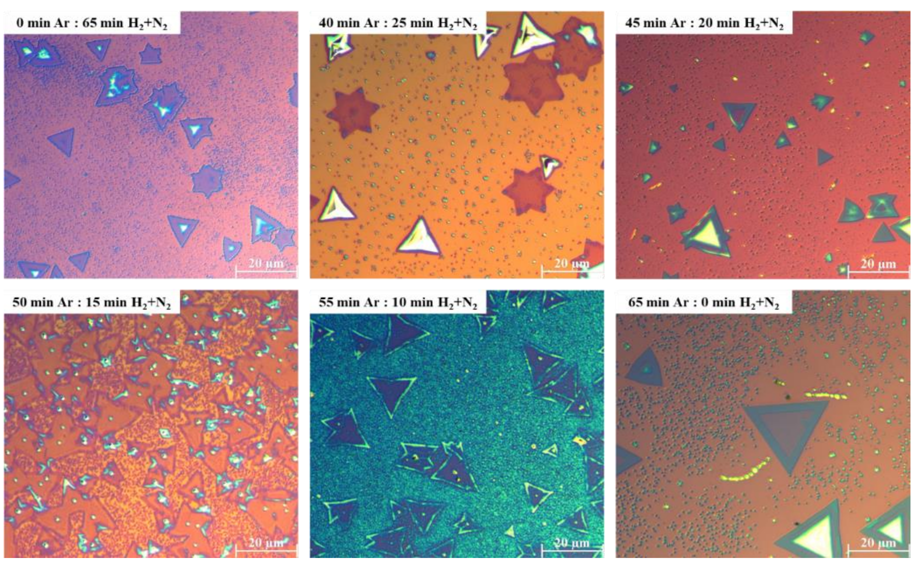

Figure 4.4 The OM morphology of contoling atomspheric condition with variation of Ar and H_2/N_2 gas supply timeslot.

	Precursor		Position and substrate		Temperature				Gas Flow	
First pot	S/mg	MoO_3/mg	Upstream	Downstream	Zone1/°C	Zone2/°C	Heating up time/min	Holding time/min	Ar/sccm	5% H_2+N_2/ sccm
	99.9	<2	/	SiO_2/Si	120	660	16	10	150	/
Second pot	S/mg	WO_3/mg	Upstream	Downstream	Zone1/°C	Zone2/°C	Heating up time/min	Holding time/min	Ar/sccm	5% H_2+N_2/sccm
	100.1	5.7	/	SiO_2/Si	180	800 (annealing) 900	40	5	250	50(switching)

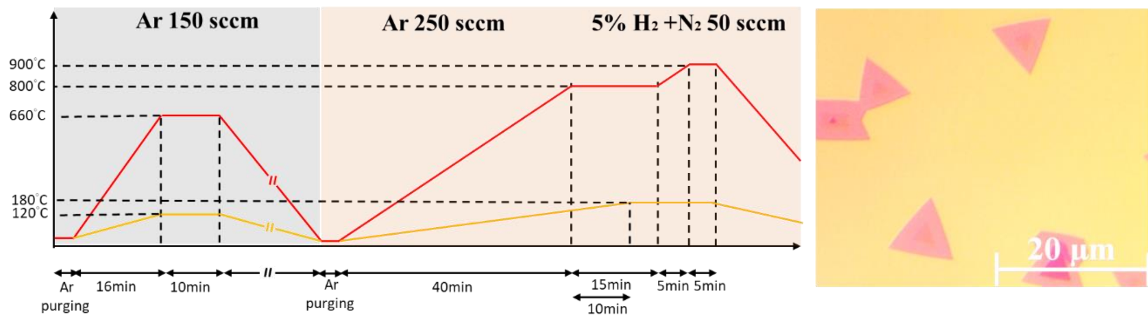

Figure 4.5 Optimized growth recipe for MoS_2-WS_2 heterostructure, temperature various time curve of CVD and the corresponding optical image.

4.2.2 Classification of MoS_2-WS_2 heterostructure

The experiment successfully achieved the synthesis of a monolayer structure consisting of a MoS_2 core and a WS_2 shield. The resulting structure exhibited a well-defined interface. which are being observed in both the optical microscope and Raman mapping results in Figure 4.2. The characteristics peak of Raman show clear distinct signal at outer edge and core structure. The peaks observed at 383.14 cm^{-1} and 400.94 cm^{-1} correspond to the fingerprint of MoS_2, specifically the E^1_{2g} and A^1_g signals. These peaks are distinguished by a difference of approximately 18-20 cm^{-1}, indicating monolayer MoS_2. The prominent peaks observed in the spectrum are located at 353.46 cm^{-1} and 417.47 cm^{-1} , which correspond to the E^1_{2g} and A^1_g peaks of WS_2 ,respectively. Layer dependence difference is not significant as MoS_2 since the overlapped of signal and other vibration modes(*71*). The obtained results indicate the presence of a lateral MoS_2-WS_2 heterostructure. However, further investigation is required to explore the interphase in detail and reveal the specific properties of the junction.

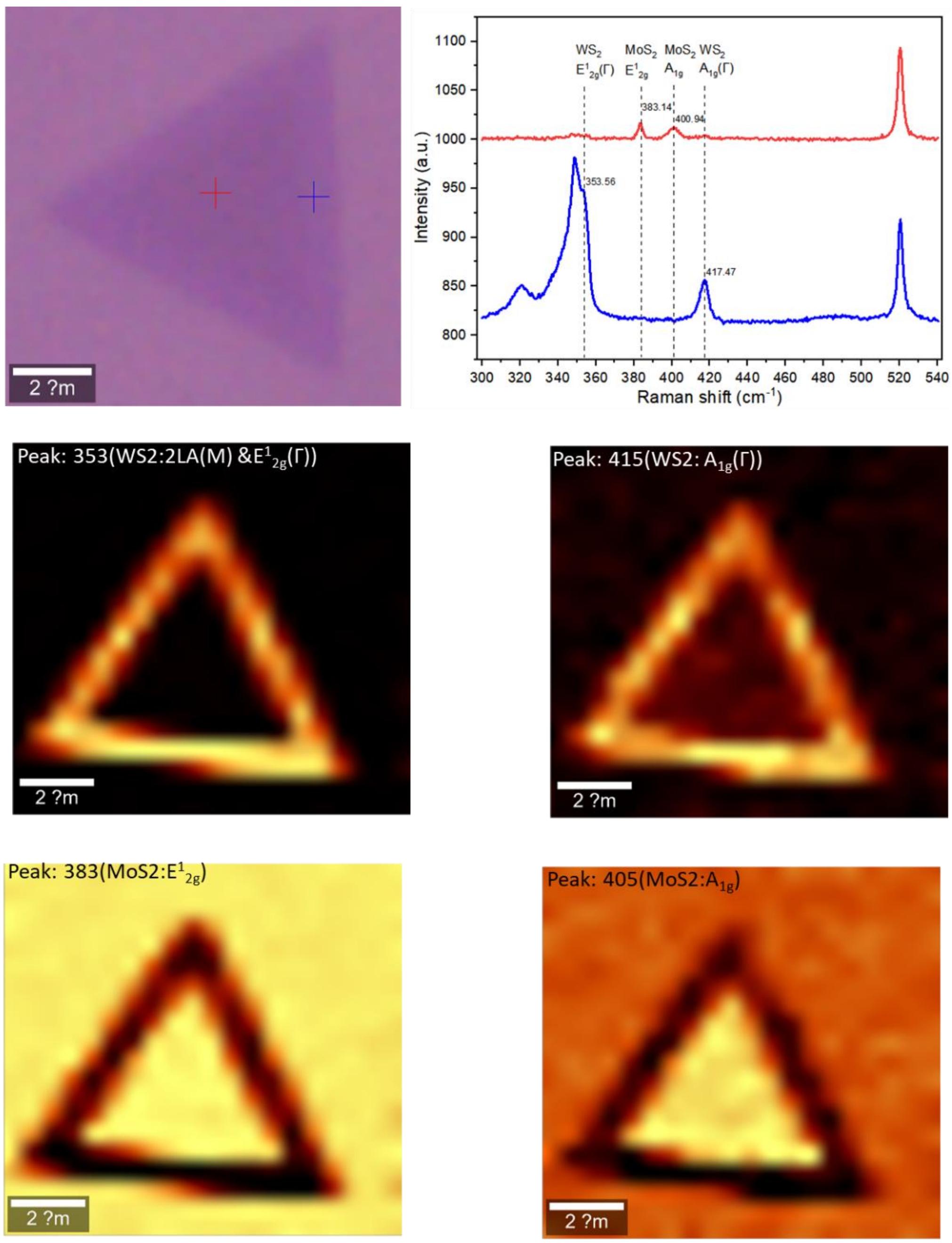

Figure 4.6 Raman spectroscopy for MoS_2-WS_2 heterostructure

4.2.3 Atomic Structure of the MoS_2-WS_2 Junction

HAADF images offer valuable insights into the crystallinity and chemical distribution at as-grown heterojunctions using sequential CVD methods. Both monolayer MoS_2 and WS_2 exhibit hexagonal arrangements with D_{3h} symmetry and form lateral heterostructure as resolved by STEM techniques. Sulfur atoms (S_2) appear with the lowest intensity, while tungsten (W) sites display twice the intensity compared to molybdenum (Mo). Notably, Figure 4.3 illustrates distinct regions of W doped MoS_2 and WS_2, corresponding to regions (3) and (1) in the figure, respectively. At the heterostructure interface marked as (2) in Figure 4.3, there is a wide distribution of Mo and W elements, indicating the formation of an alloy state, $Mo_xW_{1-x}S_2$. Interestingly, it appears that doping W into the MoS_2 core and doping Mo into the outer WS_2 layer show anisotropy of width length at the interface. The alloy state elongated its more toward the core MoS_2. It might probability imply the interfacial effect dominantly originated from W doped MoS_2 instead of Mo doped WS_2.

Controlling the interfacial width is an essential factor that influences the behavior of heterostructure systems. By employing atomic finding algorithms alongside high-resolution STEM imaging, it can identify atomic positions with high precision. This approach facilitates a analysis of elemental distribution, as depicted in Figure 4.3, where the atomic locations of W (represented by red dots) and Mo (represented by blue dots) are distinguishable.

During our analytical process, we tracked the decline of the tungsten element across the interface. The interface was determined to have an approximate width of 12nm, based on the observed reduction in tungsten concentration from 90% to 30%. This measurement not only offers a preliminary insight into the extent of intermingling between the elements from the two different TMD layers at the heterointerface but also might provide crucial information for band alignment calculations. The actual structure and width of the junction affect the junction structure, and understanding the energy level alignment between the two materials is key for comprehending charge transfer mechanisms and the overall performance of the device. Further investigation into the precise control of this interfacial width is critical. It holds the potential to tune the properties of heterostructure, which could lead to advancements in device efficiency and functionality for a wide range of applications.

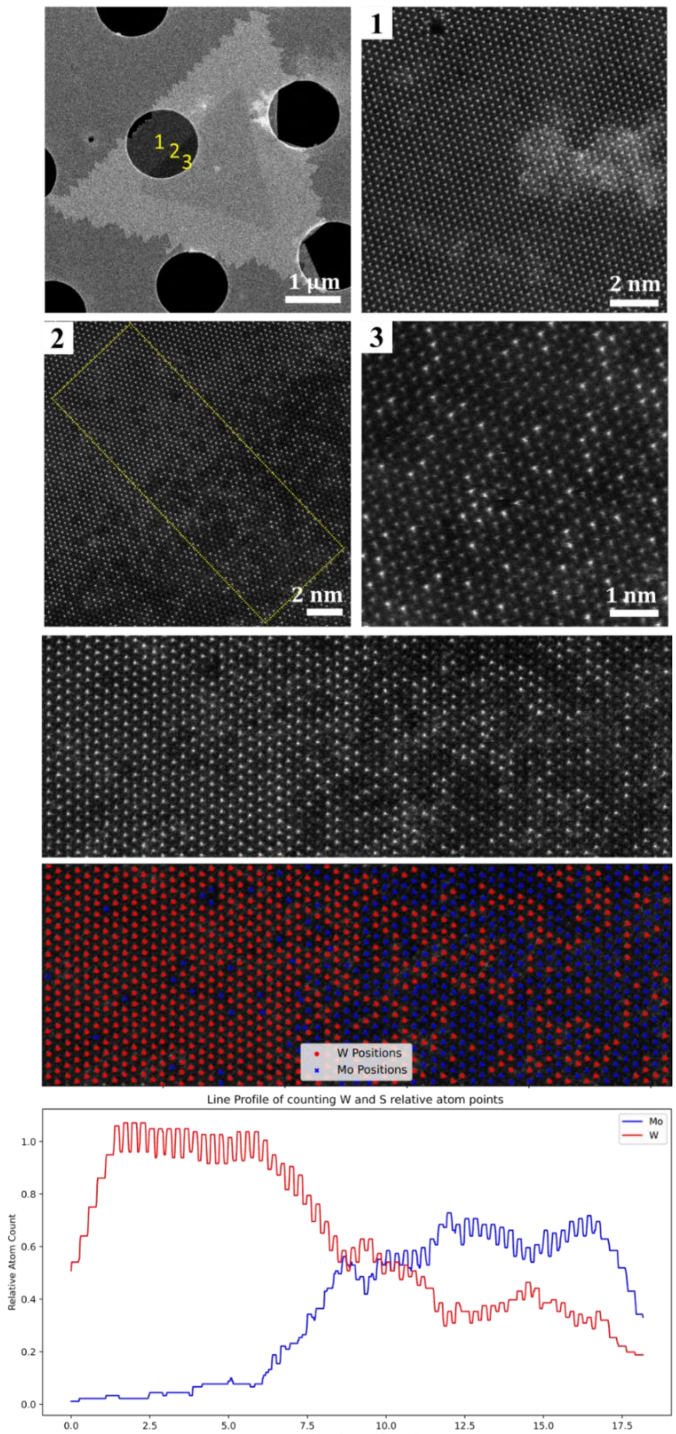

Figure 4.7 atomic resolution STEM images corresponding to the location to WS_2 shield. MoS_2-WS_2 junction, MoS_2 core. The yellow dotted marked region of interest for atomic identification. The line profile displays the variation of tungsten and molybdenum.

Chapter 5. Conclusions

2D materials have various unique properties. For example, In_2Se_3 have piezoelectricity and ferroelectricity offer the possibility to solve limitation of conventional ferroelectric oxide materials. The ferroelectric α-In_2Se_3 can be an candidate to fabricate the semiconductor ferroelectric field effect transistor that might solve the limitation in tunnelling current. Although, the doped HfO_2 show a ferroelectric in 5 nm thickness, it tends to become amorphous in further decreasing the thickness. The intrinsic stability of α-In_2Se_3 up to monolayer limit show an significant in application, while we try to investigate the ferroelectric structure with α-In_2Se_3 and β'-In_2Se_3 concerning the event of stability, where the formation of heterostructure possibility enhance the ferrelectricity due to lower structure symmetric properties. The second focus of the study the structure of interphase, as the common TMD material of MoS_2 and WS_2. These materials possess similar lattice structures and small lattice mismatches. We use sequential CVD methods integrate 2D vdW MoS2 and WS_2 interjoined together, find the different doping length within the junction that might providing insight for enhancing material properties.

The preliminary findings presented in this thesis have opened new pathways in the synthesis of MoS_2-WS_2 and phase control of α-β' In_2Se_3 heterostructures. To gain a more comprehensive understanding, more work to assess the quality of these heterostructures is crucial.

For MoS_2-WS_2 heterostructures, paramount to future research is the electronic measurement of carrier mobility, defect densities, and interfacial width. These characteristics are fundamental to understanding and optimizing the performance of device. Fabricating prototype devices that incorporate MoS_2-WS_2 heterostructures will be essential for the evaluation of quality, particularly about their junction structure. This step is not merely a means to validate the theoretical models but also a vital process to gain insights into areas ripe for improvement.

The study into α-β' In_2Se_3 heterostructures demands a focused exploration of their functional properties, with a focus on the unique phase transition behaviors of material. Comprehending the influence that these phase transitions exert on the electrical properties is a cornerstone for the invention of novel devices that can leverage these phase changes. A profound study of the ferroelectric and antiferroelectric interfaces within α-β' In_2Se_3 heterostructures will be a key aspect of upcoming investigations. Notably, the potential for α-β' phase switchable devices represents a compelling direction with significant application potential, such as memory devices, sensors, and transistors.

In essence, the future work derived from this research is expected to contribute innovative applications and deepen our comprehension of 2D materials. The promise that these heterostructures hold is immense, and the forthcoming research efforts will be pivotal in translating this potential into tangible advancements.

Reference

1. R. Baby, B. Saifullah, M. Z. Hussein, Carbon nanomaterials for the treatment of heavy metal-contaminated water and environmental remediation. *Nanoscale research letters* **14**, 1-17 (2019).
2. M. H. Kalantari, X. Zhang, Thermal Transport in 2D Materials. *Nanomaterials* **13**, 117 (2023).
3. G. Han, Z.-G. Chen, J. Drennan, J. Zou, Indium Selenides: Structural Characteristics, Synthesis and Their Thermoelectric Performances. *Small* **10**, 2747-2765 (2014).
4. T.-R. Wei *et al.*, Exceptional plasticity in the bulk single-crystalline van der Waals semiconductor InSe. *Science* **369**, 542-545 (2020).
5. R. J. Toh, Z. Sofer, J. Luxa, D. Sedmidubský, M. Pumera, 3R phase of MoS 2 and WS 2 outperforms the corresponding 2H phase for hydrogen evolution. *Chemical Communications* **53**, 3054-3057 (2017).
6. M. Yi, Z. Shen, A review on mechanical exfoliation for the scalable production of graphene. *Journal of Materials Chemistry A* **3**, 11700-11715 (2015).
7. L. Li *et al.*, Research progress of the liquid-phase exfoliation and stable dispersion mechanism and method of graphene. *Frontiers in Materials* **6**, 325 (2019).
8. J. N. Coleman *et al.*, Two-Dimensional Nanosheets Produced by Liquid Exfoliation of Layered Materials. *Science* **331**, 568-571 (2011).
9. Z. Cai, B. Liu, X. Zou, H.-M. Cheng, Chemical vapor deposition growth and applications of two-dimensional materials and their heterostructures. *Chemical reviews* **118**, 6091-6133 (2018).
10. W. Nunn, T. K. Truttmann, B. Jalan, A review of molecular-beam epitaxy of wide bandgap complex oxide semiconductors. *Journal of Materials Research* **36**, 4846-4864 (2021).
11. A. Koma, Van der Waals epitaxy for highly lattice-mismatched systems. *Journal of Crystal Growth* **201-202**, 236-241 (1999).
12. W. Choi *et al.*, Recent development of two-dimensional transition metal dichalcogenides and their applications. *Materials Today* **20**, 116-130 (2017).
13. H. Brune, "Growth modes," (Pergamon, 2001).
14. J. Valasek, Piezo-Electric and Allied Phenomena in Rochelle Salt. *Physical Review* **17**, 475-481 (1921).
15. X. Wang *et al.*, Van der Waals engineering of ferroelectric heterostructures for long-retention memory. *Nature Communications* **12**, 1109 (2021).
16. C. Dagdeviren *et al.*, Conformable amplified lead zirconate titanate sensors with enhanced piezoelectric response for cutaneous pressure monitoring. *Nature Communications* **5**, 4496 (2014).
17. Y. Li *et al.*, Enhanced bulk photovoltaic effect in two-dimensional ferroelectric CuInP2S6. *Nature Communications* **12**, 5896 (2021).
18. X. Zheng *et al.*, Phase and polarization modulation in two-dimensional In₂Se₃ via in situ transmission electron microscopy. *Science Advances* **8**, eabo0773 (2022).
19. G. E. Moore, Cramming more components onto integrated circuits. *Proceedings of the IEEE* **86**, 82-85 (1998).
20. S. Wang, X. Liu, P. Zhou, The Road for 2D Semiconductors in the Silicon Age. *Advanced Materials* **34**, 2106886 (2022).
21. K. S. Novoselov *et al.*, Electric Field Effect in Atomically Thin Carbon Films. *Science* **306**, 666-669 (2004).
22. S. Wang *et al.*, Two-dimensional devices and integration towards the silicon lines. *Nature Materials* **21**, 1225-1239 (2022).

23. Y. L. Huang *et al.*, Bandgap tunability at single-layer molybdenum disulphide grain boundaries. *Nature Communications* **6**, 6298 (2015).
24. A. K. Geim, I. V. Grigorieva, Van der Waals heterostructures. *Nature* **499**, 419-425 (2013).
25. M. Küpers *et al.*, Controlled Crystal Growth of Indium Selenide, In2Se3, and the Crystal Structures of α-In2Se3. *Inorganic Chemistry* **57**, 11775-11781 (2018).
26. M. Si *et al.*, A ferroelectric semiconductor field-effect transistor. *Nature Electronics* **2**, 580-586 (2019).
27. K. F. Mak, C. Lee, J. Hone, J. Shan, T. F. Heinz, Atomically Thin ${\mathrm{MoS}}_{2}$: A New Direct-Gap Semiconductor. *Physical Review Letters* **105**, 136805 (2010).
28. S. Cho *et al.*, Phase patterning for ohmic homojunction contact in MoTe₂. *Science* **349**, 625-628 (2015).
29. A. Chaves *et al.*, Bandgap engineering of two-dimensional semiconductor materials. *npj 2D Materials and Applications* **4**, 29 (2020).
30. Y. Liu *et al.*, Promises and prospects of two-dimensional transistors. *Nature* **591**, 43-53 (2021).
31. W. Han *et al.*, Phase-controllable large-area two-dimensional In2Se3 and ferroelectric heterophase junction. *Nature Nanotechnology* **18**, 55-63 (2023).
32. Y. Wang *et al.*, Van der Waals contacts between three-dimensional metals and two-dimensional semiconductors. *Nature* **568**, 70-74 (2019).
33. J. Wang *et al.*, Dual-coupling-guided epitaxial growth of wafer-scale single-crystal WS2 monolayer on vicinal a-plane sapphire. *Nature Nanotechnology* **17**, 33-38 (2022).
34. C. Cui *et al.*, Intercorrelated in-plane and out-of-plane ferroelectricity in ultrathin two-dimensional layered semiconductor In2Se3. *Nano letters* **18**, 1253-1258 (2018).
35. R. Rashid *et al.*, Shape-control growth of 2D-In 2 Se 3 with out-of-plane ferroelectricity by chemical vapor deposition. *Nanoscale* **12**, 20189-20201 (2020).
36. S. H. Choi *et al.*, Large-scale synthesis of graphene and other 2D materials towards industrialization. *Nature Communications* **13**, 1484 (2022).
37. M. Lin *et al.*, Controlled growth of atomically thin In2Se3 flakes by van der Waals epitaxy. *Journal of the American Chemical Society* **135**, 13274-13277 (2013).
38. D. S. Choi *et al.*, Effect of Cooling Condition on Chemical Vapor Deposition Synthesis of Graphene on Copper Catalyst. *ACS Applied Materials & Interfaces* **6**, 19574-19578 (2014).
39. D. Bufford, Y. Liu, J. Wang, H. Wang, X. Zhang, In situ nanoindentation study on plasticity and work hardening in aluminium with incoherent twin boundaries. *Nature Communications* **5**, 4864 (2014).
40. S. Alam, M. Asaduzzaman Chowdhury, A. Shahid, R. Alam, A. Rahim, Synthesis of emerging two-dimensional (2D) materials – Advances, challenges and prospects. *FlatChem* **30**, 100305 (2021).
41. W. Jianghao, L. Guangshe, L. Liping, in *Two-dimensional Materials,* N. Pramoda Kumar, Ed. (IntechOpen, Rijeka, 2016), pp. Ch. 1.
42. S. Nakamura, G. Fasol, in *The Blue Laser Diode: GaN Based Light Emitters and Lasers,* S. Nakamura, G. Fasol, Eds. (Springer Berlin Heidelberg, Berlin, Heidelberg, 1997), pp. 35-77.
43. I. Akasaki, H. Amano, Y. Koide, K. Hiramatsu, N. Sawaki, Effects of ain buffer layer on crystallographic structure and on electrical and optical properties of GaN and Ga1−xAlxN (0 < x ≦ 0.4) films grown on sapphire substrate by MOVPE. *Journal of Crystal Growth* **98**, 209-219 (1989).
44. L. A. Walsh, C. L. Hinkle, van der Waals epitaxy: 2D materials and topological insulators. *Applied Materials Today* **9**, 504-515 (2017).
45. S. Vishwanath *et al.*, Comprehensive structural and optical characterization of MBE grown MoSe2 on graphite, CaF2 and graphene. *2D Materials* **2**, 024007 (2015).
46. T. Kuech, *Handbook of Crystal Growth: Thin Films and Epitaxy*. (Elsevier, 2014).

47. G. Busch, P. Scherrer, Eine neue seignette-elektrische Substanz. *Naturwissenschaften* **23**, 737-737 (1935).
48. C. Randall, R. Newnham, L. Cross, History of the first ferroelectric oxide, BaTiO3. *Materials Research Institute, The Pennsylvania State University, University Park, Pa, USA* **1**, (2004).
49. X. Tao, Y. Gu, Crystalline–crystalline phase transformation in two-dimensional In2Se3 thin layers. *Nano letters* **13**, 3501-3505 (2013).
50. J. Van Landuyt, G. Van Tendeloo, S. Amelinckx, Phase transitions in In2Se3 as studied by electron microscopy and electron diffraction. *physica status solidi (a)* **30**, 299-314 (1975).
51. J. Liu, S. T. Pantelides, Pyroelectric response and temperature-induced α-β phase transitions in α-In2Se3 and other α-III2VI3 (III = Al, Ga, In; VI = S, Se) monolayers. *2D Materials* **6**, 025001 (2019).
52. Z. Ma, V. Skumryev, M. Gich, Magnetic properties of synthetic fluorophlogopite mica crystals. *Materials Advances* **1**, 1464-1471 (2020).
53. K. A. Pandelisev, CRYSTAL GROWTH OF SYNTHETIC FLUORIDE MICA CRYSTAL.
54. B. Li *et al.*, Probing van der Waals interactions at two-dimensional heterointerfaces. *Nature nanotechnology* **14**, 567-572 (2019).
55. Y.-H. Lee *et al.*, Synthesis of Large-Area MoS2 Atomic Layers with Chemical Vapor Deposition. *Advanced Materials* **24**, 2320-2325 (2012).
56. Q. Ji, Y. Zhang, Y. Zhang, Z. Liu, Chemical vapour deposition of group-VIB metal dichalcogenide monolayers: engineered substrates from amorphous to single crystalline. *Chemical Society Reviews* **44**, 2587-2602 (2015).
57. R. Guan *et al.*, Chemical vapor deposition of clean and pure MoS 2 crystals by the inhibition of MoO 3− x intermediates. *CrystEngComm* **23**, 146-152 (2021).
58. J. Zhou *et al.*, A library of atomically thin metal chalcogenides. *Nature* **556**, 355-359 (2018).
59. H. Di *et al.*, Controlled growth of high spatial uniformity of monolayer single crystal MoS2. *Journal of Materials Science: Materials in Electronics* **32**, 17009-17020 (2021).
60. S. Wang *et al.*, Shape Evolution of Monolayer MoS2 Crystals Grown by Chemical Vapor Deposition. *Chemistry of Materials* **26**, 6371-6379 (2014).
61. N. K. Perkgoz, M. Bay, Investigation of single-wall MoS 2 monolayer flakes grown by chemical vapor deposition. *Nano-Micro Letters* **8**, 70-79 (2016).
62. S. Li *et al.*, Wafer-scale and deterministic patterned growth of monolayer MoS 2 via vapor–liquid–solid method. *Nanoscale* **11**, 16122-16129 (2019).
63. B. Shi *et al.*, High-efficiency synthesis of large-area monolayer WS2 crystals on SiO2/Si substrate via NaCl-assisted atmospheric pressure chemical vapor deposition. *Applied Surface Science* **533**, 147479 (2020).
64. S. Li *et al.*, Halide-assisted atmospheric pressure growth of large WSe2 and WS2 monolayer crystals. *Applied Materials Today* **1**, 60-66 (2015).
65. G. Zhang *et al.*, Synthesis of centimeter-scale WS2 membrane by chemical vapor deposition. *Journal of Materials Science: Materials in Electronics* **33**, 22560-22572 (2022).
66. F. Lan *et al.*, Controllable synthesis of millimeter-size single crystal WS2. *Applied Surface Science* **504**, 144378 (2020).
67. Y. Xie *et al.*, NaCl-assisted CVD synthesis, transfer and persistent photoconductivity properties of two-dimensional transition metal dichalcogenides. *MRS Advances* **3**, 365-371 (2018).
68. Y. Xie *et al.*, Growth of monolayer WS2 single crystals with atmospheric pressure CVD: Role of temperature. *MRS Advances* **4**, 255-262 (2019).
69. Z. Wang *et al.*, NaCl-assisted one-step growth of MoS2–WS2 in-plane heterostructures. *Nanotechnology* **28**, 325602 (2017).
70. D. Dumcenco *et al.*, Large-area epitaxial monolayer MoS2. *ACS nano* **9**, 4611-4620 (2015).

71. A. Berkdemir *et al.*, Identification of individual and few layers of WS2 using Raman Spectroscopy. *Scientific Reports* **3**, 1755 (2013).